

# Tightening Cosmological Constraints Within and Beyond $\Lambda$ CDM Using Gamma-Ray Bursts Calibrated with Type Ia Supernovae

Wei Hong<sup>1,2,3</sup>, Luca Izzo<sup>1,\*</sup>, Massimo Della Valle<sup>4</sup>, Orlando Luongo<sup>5,6,7,8,9</sup>, Marco Muccino<sup>5,9,10</sup>, and Tong-Jie Zhang<sup>2,3</sup>

<sup>1</sup> INAF - Osservatorio Astronomico di Capodimonte, Salita Moiariello 16, I-80131 Napoli, Italy

<sup>2</sup> Institute for Frontiers in Astronomy and Astrophysics, Beijing Normal University, Beijing 102206, China

<sup>3</sup> Department of Astronomy, Beijing Normal University, Beijing 100875, China

<sup>4</sup> INAF - Osservatorio Astronomico di Padova, Vicolo dell'Osservatorio 5, I-35122 Padova, Italy

<sup>5</sup> Università di Camerino, Via Madonna delle Carceri, Camerino, 62032, Italy

<sup>6</sup> INAF - Osservatorio Astronomico di Brera, Milano, Italy

<sup>7</sup> Istituto Nazionale di Fisica Nucleare, Sezione di Perugia, Perugia, 06123, Italy

<sup>8</sup> SUNY Polytechnic affiliation, 13502 Utica, New York, USA

<sup>9</sup> Al-Farabi Kazakh National University, Al-Farabi av. 71, 050040 Almaty, Kazakhstan

<sup>10</sup> ICRA Net, Piazza della Repubblica 10, 65122 Pescara, Italy

Received XX XX, 20XX

## ABSTRACT

**Context.** Gamma-ray bursts (GRBs) reach redshifts beyond Type Ia supernovae (SNe Ia) and can extend distance measurements into the early Universe, but their use as distance indicators is limited by the circularity problem in calibrating empirical luminosity relations.

**Aims.** We present a model-independent methodology to overcome this circularity by combining Pantheon+ SNe Ia, a distance reconstruction based on artificial neural networks (ANNs), and two GRB correlations (Amati and Combo) into a distance ladder from low to high redshift, with the goal of constraining cosmological parameters in  $\Lambda$ CDM and  $w_0w_a$ CDM.

**Methods.** We use the ReFANN to reconstruct the luminosity distance  $d_L(z)$  and distance modulus  $\mu(z)$  from the Pantheon+ dataset, with hyperparameters optimized via approximate Bayesian computation rejection and a risk function. This model-independent reconstruction calibrates the Amati and Combo relations using a low-redshift ( $z < 1$ ) GRB sample from Fermi GBM and Swift-XRT. The calibrated relations then provide distance estimates for GRBs at  $z \geq 1$ . Finally, a joint Bayesian analysis simultaneously constrains the cosmological and GRB correlation parameters, ensuring self-consistent uncertainty propagation.

**Results.** We obtain consistent cosmological constraints from two independent GRB correlations. The Hubble constant  $H_0$  agrees with SNe Ia values, though potentially influenced by Pantheon+ dataset. High-redshift GRBs favour a higher matter density  $\Omega_m$  than the Pantheon+ and hint at possible dark energy evolution.

**Conclusions.** We present a framework that mitigates GRB cosmology's circularity problem, extending the distance ladder to  $z \sim 9$  and establishing GRBs as a high-redshift probe.

**Key words.** cosmological parameters – Gamma-ray burst: general – supernovae: general – dark energy

## 1. Introduction

Observational cosmology has recently entered into the era of precision measurement (Weinberg et al. 2013; Maartens et al. 2015). The cosmological parameters, including the Hubble constant  $H_0$ , the matter density parameter  $\Omega_m$ , and the dark energy equation-of-state parameters  $w_0$  and  $w_a$  in the  $w_0w_a$ CDM, can be measured with exceptional precision through various probes now. However, significant tensions remain among different observations, such as the difference in  $H_0$  between local distance-ladder measurements and CMB-inferred values. A central question in modern cosmology is how to evaluate the constraining ability of various data sets on cosmological parameters in a model-independent manner (Luongo & Muccino 2023; Muccino et al. 2023; Luongo & Muccino 2020). Among the many cosmological probes, SNe Ia play a crucial role at low redshift owing to their well-established standard-candle prop-

erties (Phillips 1993). But, the redshift distribution of current SNe Ia samples is mostly confined to  $z \leq 2$ , and the data become sparse with larger statistical uncertainties in the high-redshift regime  $z > 1$  (Malmquist 1922). As a result, SNe Ia alone cannot provide tight constraints on the expansion history and dark energy evolution at  $z \geq 1$ . Extending the distance ladder to higher redshift therefore requires introducing intrinsically brighter objects as complementary probes. In recent years, a number of such "beyond-standard" cosmological probes have been developed to validate results and control systematics, as reviewed by Moresco et al. (2022). Among these, gamma-ray bursts (GRBs) are a class of highly energetic transients whose peak luminosities far exceed those of ordinary supernovae, allowing them to be detected out to redshifts of  $z \sim 1 - 9$  or even beyond (Piran 2004; Mészáros 2006; Tanvir & Jakobsson 2007; Tanvir et al. 2009; Salvaterra et al. 2009; Gehrels et al. 2009; Cucchiara et al. 2011). Consequently, GRBs have long been proposed as promising standardisable candles at high redshift (Dai et al. 2004; Ghirlanda et al. 2004; Liang & Zhang 2005;

\* luca.izzo@inaf.it

Schaefer 2007; Izzo et al. 2009; Cardone et al. 2009; Wang et al. 2015; Demianski et al. 2017; Dainotti et al. 2017). At the same time, GRBs involve complex emission physics and exhibit intrinsic luminosities spanning several orders of magnitude with a highly dispersed distribution. Hence, one must rely on empirical correlations, such as the Amati relation (Amati et al. 2002; Amati 2006; Amati et al. 2008) or the Yonetoku relation (Yonetoku et al. 2004; Ghirlanda et al. 2005; Yonetoku et al. 2010), to find a relationship between the equivalent isotropic radiated energy and cosmology before using GRBs for cosmological parameter constraints (Schaefer 2007; Amati & Della Valle 2013; Luongo & Muccino 2021a).

The Amati relation, connecting the rest-frame spectral peak energy  $E_{p,i}$  to the isotropic-equivalent energy  $E_{\text{iso}}$ , is a widely-used empirical correlation for GRBs (Amati et al. 2002; Amati 2006; Amati et al. 2008). Given a GRB's redshift  $z$ ,  $E_{p,i}$ , and fluence  $S_{\text{obs}}$ , one can calibrate its luminosity distance  $d_L$  using the Amati parameters, enabling the construction of a high-redshift ( $z \geq 2$ ) Hubble diagram to constrain cosmology (Schaefer 2007; Mosquera Cuesta et al. 2008; Demianski & Piedipalumbo 2011). However, its traditional application suffers from a fundamental circularity problem (Liang et al. 2008; Capozziello & Izzo 2010; Demianski & Piedipalumbo 2011; Graziani 2011; Amati et al. 2019): the relation is typically calibrated by assuming a fiducial cosmological model to compute  $E_{\text{iso}}$  for low- $z$  GRBs, and then the calibrated relation is applied to high- $z$  GRBs to constrain other models. This makes the cosmological results dependent on the initial assumptions.

Unlike the Amati relation, the Combo relation offers an alternative empirical approach that builds a more robust distance indicator by combining prompt and afterglow observations (Amati et al. 2008; Bernardini et al. 2012; Izzo et al. 2015; Muccino et al. 2021). It connects the rest-frame X-ray afterglow plateau luminosity  $L_0$  to three prompt/afterglow parameters: the spectral peak energy  $E_{p,i}$ , the plateau duration  $\tau$ , and the post-plateau decay index  $\alpha_{PL}$ , via  $\log L_0 = \log A + \gamma \log E_{p,i} - \log[\tau/(1 + \alpha_{PL})]$  (Margutti et al. 2013; Ruffini et al. 2014). From measurements of  $E_{p,i}$ ,  $\tau$ ,  $\alpha_{PL}$ , and the observed flux  $F_0$ , one can derive  $d_L$  using a calibrated Combo relation. This extends the GRB Hubble diagram to the entire observable redshift range (up to  $z \sim 9$ ), providing a unique probe for high-redshift dark energy studies.

Building upon such calibrations, the Combo relation has been applied to constrain the dark energy equation of state  $w(z) = w_0 + w_a z/(1 + z)$  (Chevallier & Polarski 2001; Linder 2003). Due to the scarcity of low-redshift GRBs, a redshift-binned approach is often adopted (Muccino et al. 2021; Luongo & Muccino 2021a). Although this approach yields preliminary constraints, it suffers from several limitations. The bin choice is often subjective, lacking clear optimization criteria (Huterer & Starkman 2003; Wang & Tegmark 2004; Seikel et al. 2012). More critically, uncertainties propagate and amplify from lower to higher redshift bins, making high- $z$  constraints fragile. Additionally, the results are sensitive to the intrinsic scatter of GRBs and to outliers or selection effects (Butler et al. 2009; Dainotti et al. 2015; Petrosian et al. 2015; Dainotti & Amati 2018). Therefore, traditional binning is limited by the relation's scatter, residual model dependencies, and the binning process itself. This underscores the need for a model-independent approach that can account for complex correlations without predefined parametric forms or binning.

To alleviate the aforementioned issues, a common approach is to use the SNe Ia distance scale to non-parametrically

reconstruct the relationships  $d_L(z)$  and  $\mu(z)$ , which then calibrate low-redshift GRB distances for empirical relations like Amati and Combo, avoiding specific cosmological parameterizations (Shafieloo et al. 2006; Liang et al. 2008; Capozziello & Izzo 2010). Such model-independent reconstructions have been explored using Gaussian processes (Rasmussen & Williams 2006; Shafieloo et al. 2012; Seikel et al. 2012, 2013; Salzano et al. 2015; Sun et al. 2021; Hwang et al. 2023; Zhang et al. 2023, 2024a), non-parametric regression (Shafieloo et al. 2006; Shafieloo 2007; Holsclaw et al. 2010, 2011; Zhang et al. 2024b), and machine-learning techniques (Luongo & Muccino 2021b; Dialektopoulos et al. 2023; Gómez-Vargas et al. 2023; Hong et al. 2023; Chen et al. 2025). In this paper, we employ artificial neural networks (ANNs) for this reconstruction. And there are three reasons for us to employ the ANNs. First, they provide flexible yet well-controlled reconstructions of both  $d_L(z)$  and  $\mu(z)$ . Second, ANNs scale favorably to large and heterogeneous supernova compilations. Third, they allow for an objective treatment of network and hyperparameter uncertainty within our approximate Bayesian computation framework. Unlike standard Gaussian process reconstructions that depend sensitively on kernel choices and scale as order  $N$  cubed with the number of supernovae unless approximations are employed, feed-forward ANNs learn the mapping directly from data without assuming any specific covariance form. Compared to generic nonparametric regression methods such as splines or local polynomials, ANNs can naturally incorporate physically motivated regularities like smoothness and monotonicity, and they facilitate uncertainty propagation into subsequent GRB calibrations. Importantly, by coupling ANNs with risk-function evaluation and an ABC rejection scheme, we marginalize over candidate networks, reduce subjective tuning, and obtain a reproducible pipeline that quantifies how hyperparameter choices affect the reconstructed distances. Using the Pantheon+ SNe Ia sample (Brout et al. 2022; Scolnic et al. 2022) and the ReFANN framework (Wang et al. 2020), we obtain  $d_L(z)$  and  $\mu(z)$  without relying on models like  $\Lambda$ CDM. To objectively determine the optimal network and mitigate the uncertainty from hyperparameter choice, we integrate risk-function evaluation (Vapnik 1999; Wasserman et al. 2001) with an approximate Bayesian computation (ABC) rejection approach. For model comparison within ABC, we use goodness-of-fit statistics (Jennings & Madigan 2017; Alsing et al. 2018, 2019; Bernardo & Levi Said 2021; Zhang et al. 2023), including a composite metric similar to the log marginal likelihood (Abdesslem et al. 2017; Gómez-Valent & Amendola 2018). The ABC framework itself is informed by established sampling and model selection principles (Beaumont et al. 2008; Trotta 2008; Cornuet et al. 2008; Weyant et al. 2013; Beaumont 2019). This systematic process reduces subjectivity in model selection. Instead of manually selecting networks through qualitative inspection, each candidate network is evaluated using a defined risk function and subjected to a consistent ABC rejection criterion. The procedure effectively marginalizes over a wide hyperparameter space and propagates the resulting model selection uncertainty into the reconstructed  $d_L(z)$  and  $\mu(z)$  relations.

After selecting the optimal ReFANN, we calibrate the Amati and Combo relations using the reconstructed  $d_L(z)$  and  $\mu(z)$  for low-redshift GRBs. Their parameters are fitted via Bayesian inference (Bloom et al. 2001) with MCMC sampling (Metropolis et al. 1953; Hastings 1970; D'Agostini 2005; Kelly 2007), accounting for observational uncertainties and intrinsic scatter  $\sigma_{\text{cal}}$  specific to each relation. The calibrated relations

then provide distance estimates for high-redshift GRBs. Crucially, we perform a hierarchical Bayesian analysis that simultaneously samples cosmological parameters ( $H_0, \Omega_m, \Omega_\Lambda, w_0, w_a$ ) alongside the Amati ( $A_A, \gamma_A, \sigma_{\text{cal}}^A$ ) and Combo ( $A_C, \gamma_C, \sigma_{\text{cal}}^C$ ) parameters, integrating Pantheon+ and GRB distances within a combined framework that avoids the circularity of traditional two-step calibration (Amati et al. 2019). We apply this framework to both flat  $\Lambda$ CDM (Peebles 1982) and  $w_0 w_a$ CDM (Chevallier & Polarski 2001; Linder 2003) to assess robustness. It is important to note that GRB constraints on  $H_0$  are informed by the Pantheon+ calibration at low-redshifts. Without direct local anchors, GRBs should primarily be regarded as tools for characterizing dark energy, particularly its equation-of-state parameters.

The rest of the paper is organised as follows. In Sect. 2, we describe the Pantheon+ SNe Ia data and GRB samples, including selection criteria and key physical quantities with their uncertainties. In Sect. 3, we present the ANN methodology for reconstructing  $d_L(z)$  and  $\mu(z)$ , with ABC rejection sampling and risk-function evaluation for hyperparameter optimization. In Sect. 4, we present the calibration of the Amati and Combo relations using the reconstructed distances through ANN, construct the high-redshift GRB distance diagram, and report the cosmological constraints from a hierarchical Bayesian analysis under the flat  $\Lambda$ CDM and  $w_0 w_a$ CDM. Sect. 5 discusses the main findings, discusses systematic uncertainties and limitations, and outlines future extensions of the framework. Finally, Section 6 summarizes the conclusions.

## 2. Data Sets and Pre-processing

This section provides a detailed description of the observational data sets used in this work and the corresponding pre-processing procedures. Our analysis is based on two main data sources: the Pantheon+ SNe Ia sample and the Fermi GBM Burst and Swift-XRT samples (Meegan et al. 2009; Paciesas et al. 2012; von Kienlin et al. 2014; Narayana Bhat et al. 2016; von Kienlin et al. 2020; Goldstein et al. 2012; Gruber et al. 2014; Poolakkil et al. 2021). From the Pantheon+ data release (Brout et al. 2022; Scolnic et al. 2022), we extract for each supernova the following information: (a) redshift  $z$ , we preferentially adopt the cosmological redshift  $z_{\text{HD}}$ , corrected for the host-galaxy environment and peculiar velocities. (b) Distance modulus  $\mu_{\text{SNe}}$  and its uncertainty  $\sigma_{\mu_{\text{SNe}}}$ . The SNe Ia data used in this paper contains more than 1500 uniformly processed SNe Ia and is among the largest and most precise public SNe Ia data sets currently available. The redshift coverage extends from the nearby Universe ( $z \sim 0.001$ ) out to  $z \sim 2.261$ , providing a solid basis for constructing the distance-redshift relation. The Pantheon+ sample serves dual purposes in our analysis. First, it provides the empirical foundation for reconstructing a model-independent luminosity distance  $d_L(z)$  and distance modulus  $\mu(z)$ , by serving as the training and validation set for our ReFANN. This approach allows the  $d_L(z)$  and  $\mu(z)$  to be derived directly from data, without imposing a predetermined parametric cosmological model. Second, in the final hierarchical Bayesian framework, the Pantheon+ distance modulus supply robust, low-redshift cosmological constraints. They are incorporated directly into the joint likelihood function alongside GRB data, enabling a self-consistent and simultaneous constraint on both the Amati and Combo relation parameters and the underlying cosmological parameters.

The Pantheon+ dataset provides a covariance matrix  $\mathbf{C}_\mu$  of SNe Ia's distance modulus that includes both statistical and sys-

tematic uncertainties. Therefore, the luminosity distance  $d_{L,i}$  and its error  $\sigma_{d_{L,i}}$  are obtained through error propagation

$$d_{L,i} = 10^{\left(\frac{\mu_i - 25}{5}\right)} \text{Mpc}, \quad (1)$$

$$\sigma_{d_{L,i}} = \sqrt{(\mathbf{C}_{d_L})_{ii}} = \frac{\ln 10}{5} d_{L,i} \sqrt{(\mathbf{C}_\mu)_{ii}},$$

where covariance matrix of luminosity distance  $\mathbf{C}_{d_L} = \mathbf{J} \mathbf{C}_\mu \mathbf{J}^T$ , and Jacobian matrix is  $\mathbf{J} = \text{diag}\left(\frac{\partial d_{L,i}}{\partial \mu_i}\right) = \text{diag}\left(\frac{\ln 10}{5} d_{L,i}\right)$ .

The GRB sample used in this work is primarily based on observations from the Fermi GBM and Swift-XRT, combining prompt emission and X-ray afterglow data from Izzo et al. (2015) and Muccino et al. (2021). This ensures that the sample is directly suitable for calibrating both the Amati relation and the Combo relation, which relies specifically on Swift-XRT afterglow measurements. With its broad energy coverage and time resolution, Fermi GBM can robustly fit GRB spectra and provide key spectral parameters. Since the Amati empirical correlation is mainly established and tested for long GRBs ( $T_{90} > 2$  s), we impose the following physical and data-quality criteria at the initial selection stage to ensure the reliability of the subsequent analysis: (a) Reliable redshift measurements. Each GRB must have a well-determined cosmological redshift  $z_{\text{GRB}}$ , explicitly reported in the literature or in curated GRB databases. (b) Complete spectral information. We have filtered the data provided by the observed fluence  $S_{\text{obs}}$  and the observed-frame spectral peak energy  $E_{p,\text{obs}}$  together with their  $1\sigma$  statistical uncertainty  $\sigma_{S_{\text{obs}}}$  and  $\sigma_{E_{p,\text{obs}}}$ , respectively. Moreover, the time-integrated spectrum of the GRB must be well fitted by a Band function, and the fit must provide the low-energy spectral index  $\alpha$  and high-energy spectral index  $\beta$  together with their  $1\sigma$  statistical uncertainty  $\sigma_\alpha$  and  $\sigma_\beta$ , respectively. (c) Strict data-quality control. We discard events with failed spectral fits or with huge relative uncertainties, which are relative errors of order  $\geq 100\%$ , as mentioned above, so as to ensure the robustness of the input data.

To convert the observables into the rest-frame quantities required by the Amati relation, we first compute the rest-frame spectral peak energy

$$E_{p,i} = E_{p,\text{obs}} (1 + z_{\text{GRB}}), \quad (2)$$

where  $E_{p,\text{obs}}$  is the observed-frame peak energy and  $z_{\text{GRB}}$  is the GRB redshift. The corresponding uncertainty in logarithmic space is approximated by

$$\sigma_{\log_{10} E_{p,i}} = \frac{1}{\ln 10} \frac{\sigma_{E_{p,i}}}{E_{p,\text{obs}} (1 + z_{\text{GRB}})}, \quad (3)$$

with  $\sigma_{E_p}$  the  $1\sigma$  uncertainty on  $E_{p,\text{obs}}$ . Next, in order to obtain the bolometric fluence  $S_{\text{bol}}$ , we follow the procedure outlined in Schaefer (2006). Given the observed fluence  $S_{\text{obs}}$  in the instrumental energy band and an appropriate spectral model that fits the data, the bolometric fluence is estimated via (Schaefer 2007)

$$S_{\text{bol}} = S_{\text{obs}} \frac{\int_{1/(1+z)}^{10^4/(1+z)} E \Phi(E) dE}{\int_{E_{\text{min}}}^{E_{\text{max}}} E \Phi(E) dE}, \quad (4)$$

where  $(E_{\text{min}}, E_{\text{max}})$  denotes the detector energy range, and for the Fermi GBM bursts used in this work it corresponds to the nominal GBM energy band (10, 1000) keV. The function  $\Phi(E)$  is the photon spectrum adopted to fit the GRB data. In this paper we use the Band function, written as (Band et al. 1993)

$$\Phi(E) = \begin{cases} \tilde{A} E^\alpha \exp\left[-(2 + \alpha)E/E_{p,\text{obs}}\right], & \text{if } E \leq \left[\frac{\alpha - \beta}{2 + \alpha}\right] E_{p,\text{obs}}, \\ \tilde{B} E^\beta, & \text{otherwise,} \end{cases}$$

(5)

where  $\tilde{A}$  and  $\tilde{B}$  are normalisation constants,  $\alpha$  and  $\beta$  are the low- and high-energy spectral indexes.

Once the bolometric fluence  $S_{\text{bol}}$  has been estimated for each GRB in the sample within the rest-frame energy band of  $1 - 10^4$  KeV, we can compute the isotropic equivalent radiated energy  $E_{\text{iso}}$  using the famous relation between luminosity distance and fluence (Amati et al. 2002; Amati 2006; Amati et al. 2008)

$$E_{\text{iso}} = \frac{4\pi d_L^2 S_{\text{bol}}}{1 + z_{\text{GRB}}}. \quad (6)$$

The determination of luminosity distances depends clearly on the redshift of each GRB. For low-redshift GRBs ( $z_{\text{GRB}} < z_{\text{cut}} = 1$ ), the luminosity distance  $d_L$  is derived directly from the model-independent  $d_L(z)$  relation reconstructed via ANN from the Pantheon+ SNe Ia data set, as described in Sect. 3. This is due to the fact that, in the redshift range  $z < 1$ , the SNe Ia data set contains significantly more data points and exhibits substantially smaller observational uncertainties than in the  $z > 1$  regime. For high-redshift GRBs ( $z_{\text{GRB}} \geq z_{\text{cut}}$ ), the luminosity distance  $d_L$  is derived in Sect. 4 by applying the Amati relation calibrated on the low-redshift GRB subsample, using the observed rest-frame peak energy  $E_{p,i}$  and bolometric fluence  $S_{\text{bolo}}$  to calibrate their energetics.

Similar to the Amati relation, applying the Combo relation requires deriving a specific set of rest-frame parameters from observational data. Since these calculations and fits have already been systematically performed by Muccino et al. (2021) using a carefully curated GRB sample. Consequently, this work directly adopts their published, uniformly processed parameter values, which include the rest-frame peak energy  $E_{p,i}$ , the plateau flux  $F_0$ , the rest-frame plateau duration  $\tau$ , and the decay index  $\alpha$ . This approach ensures consistency in data origin and methodology, and allows us to concentrate on the cosmological analysis.

For GRBs at low redshift, the distance modulus  $\mu(z)$  is obtained directly from the model-independent  $\mu(z)$  relation reconstructed via artificial neural networks from the Pantheon+ SNe Ia data set, as described in Sect. 3. Using this low-redshift subset, characterized by its observed quadruple ( $E_{p,i}, F_0, \tau, \alpha_{PL}$ ), we can calibrate the Combo relation (Izzo et al. 2015; Muccino et al. 2021)

$$\mu_{\text{GRB}} = -97.45 + \frac{5}{2} \left[ \log \left( \frac{A_C}{\text{erg s}^{-1}} \right) + \gamma_C \log \left( \frac{E_{p,i}}{\text{keV}} \right) - \log \left( \frac{\tau/\text{s}}{|1 + \alpha_{PL}|} \right) - \log \left( \frac{F_0}{\text{erg cm}^{-2} \text{ s}^{-1}} \right) - \log 4\pi \right], \quad (7)$$

thereby determining its slope  $\gamma_C$ , normalization  $A_C$ , and intrinsic scatter  $\sigma_{\text{ex}}$ . For GRBs at high redshift ( $z \geq z_{\text{cut}}$ ), the distance modulus  $\mu(z)$  is derived in Sect. 3 by inverting the calibrated Combo relation. This methodology parallels the logic of the Amati relation but relies on a distinct empirical correlation involving different observables, providing an independent and complementary distance probe for cosmological studies.

### 3. ANN Model Optimization and Distance Reconstruction

This section presents the fundamental methodology employed in this work to reconstruct the luminosity distance  $d_L(z)$ , specifically using an ANN. It demonstrates the integration of ABC-rejection with a risk function to facilitate systematic hyperparameter optimisation and model selection within the ReFANN

framework. The optimised ReFANN is then employed to obtain a non-parametric reconstruction of  $d_L(z)$ , together with a quantitative estimate of its uncertainties. To quantify the uncertainty of the reconstructed distance relation, we combine the measurement uncertainty of the SNe Ia data with the model variance estimated from an ensemble of accepted networks. Full mathematical details and explicit definitions of this procedure are provided in Appendix A.

Conventional GRB distance-calibration procedures typically assume a parametric cosmology to compute  $d_L(z)$  and fit the Amati relation. While practical, this approach ties the results to the chosen functional form and makes it difficult to separate cosmological assumptions from the correlation parameters themselves. Here we instead calibrate low-redshift GRBs directly against the distance scale provided by Pantheon+ SNe Ia, using ReFANN to reconstruct  $d_L(z)$  nonparametrically and then evaluating it at the redshifts of low- $z$  GRBs. Any external calibrator inevitably transfers its residual systematics, but our reconstruction is restricted to  $z \leq 1$ , where Pantheon+ is dense and the distance-redshift relation is empirically well determined. Importantly, we do not treat the supernova distances as fixed inputs: reconstruction uncertainties propagate into the GRB calibration, and all cosmological and correlation parameters are inferred jointly within a single hierarchical Bayesian framework. Combined with ABC model selection and risk-function ranking for the network, this approach minimizes subjective choices and ensures that calibration uncertainties are fully carried through to the GRB distance estimates.

However, the ANN itself, such as the number of hidden layers  $N_{\text{hl}}$ , number of neurones  $N_{\text{node}}$ , activation functions and optimiser, creates a new hyperparameter space. Without a systematic model comparison and selection procedure, these design choices become implicit priors and may compromise the objectivity of the results. To address this, we impose two key optimisation criteria for ReFANN, especially the number of layers and the number of neurones.

First, within the ABC rejection, we treat different networks as distinct candidate models. For each, we compute three summary statistics on a validation set: the goodness of fit  $\chi^2$  (Bernardo & Levi Said 2021), the Euclidean distance between predictions and observations (Jennings & Madigan 2017; Zhang et al. 2023), and an approximate log marginal likelihood (LML) (Abdessalem et al. 2017; Gómez-Valent & Amendola 2018; Bernardo & Levi Said 2021). Candidate networks are then accepted or rejected based on an observable-dependent tolerance threshold  $\varepsilon$ . Detailed definitions of these statistics and the acceptance criterion are provided in Appendix A. The choice of  $\varepsilon$  is critical. If  $\varepsilon$  is too large, nearly all proposals are accepted, making the posterior distributions of different hyperparameters indistinguishable. If  $\varepsilon$  is too small, too few samples are retained, causing accepted particles to cluster too tightly exploration of the hyperparameter space. In practice, we therefore adopt an iterative procedure: starting from a high value, we gradually lower  $\varepsilon$  while monitoring the resulting posterior distributions of the hyperparameters. We identify an optimal tolerance  $\varepsilon^*$  as the value below which further reduction no longer produces significant shifts in the posteriors. This approach balances reliable inference with computational efficiency in the ABC rejection sampling. Second, following the original ReFANN, we further rank the accepted models using a risk function and Bayes-factor comparisons to identify a compact set of optimal hyperparameters (Vapnik 1999; Wasserman et al. 2001). The definitions of these quantities and the adopted interpretation scale are given in Appendix A.

Given that all distance reconstructions in this work are based on a unified methodology, the reconstruction of the distance modulus  $\mu(z)$  follows the same ANN pipeline and optimization strategy as that for the luminosity distance  $d_L(z)$ . Accordingly, using the Pantheon+ SNe Ia data set, we train a separate ReFANN network that provides a non-parametric mapping from redshift  $z$  to distance modulus  $\mu(z)$ . Hyperparameter optimization, model selection, and uncertainty quantification are carried out strictly under the ABC-rejection and risk-function criteria described in this section and include both the data error  $\sigma_{\mu,data}$  and the model error  $\sigma_{\mu,model}$ . The only substantive difference is the choice of target variable. All algorithmic steps used for  $d_L(z)$ , including the ABC distance metrics, risk-function evaluation, and Bayes-factor comparisons, are applied in an equivalent manner in the  $\mu(z)$  space. In this way, we obtain a model-independent reconstruction of  $\mu(z)$  together with its full covariance, based on the same statistical framework as the  $d_L(z)$  reconstruction.

Figure 1 illustrates the ensemble of ANN reconstructions for the distance modulus  $\mu(z)$  obtained with different ReFANN hyper-parameters. Most candidates reproduce the Pantheon+ trend at  $z \lesssim 1$ , while their extrapolations can diverge at higher redshift; a small subset yields unphysical behaviors. To avoid propagating such failures into the subsequent ABC selection, we pre-screen candidate networks using the final training loss (threshold  $\leq 0.03$  for  $\mu$ ; the companion  $d_L$  reconstruction is screened with a threshold  $\leq 0.4$ ). The full set of luminosity-distance reconstructions is provided in Appendix Fig. A.1.

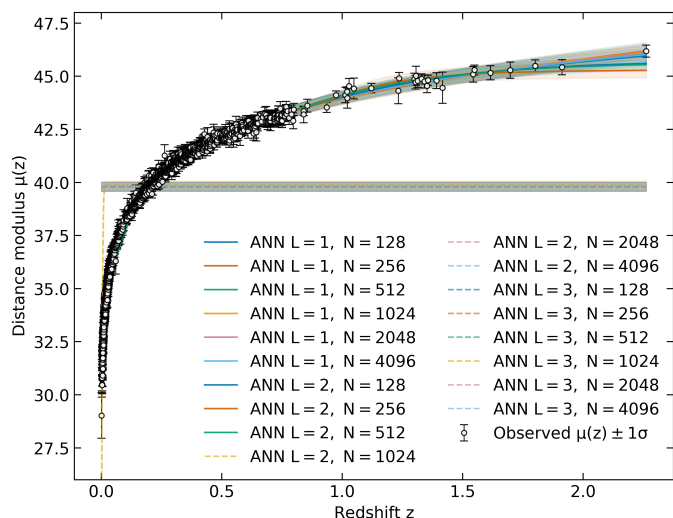


Fig. 1: The reconstructed distance modulus  $\mu(z)$  using ReFANN with different network hyperparameters. Each line corresponds to a different combination of the number of hidden layers ( $N_{hi}$ ) and the number of nodes per layer ( $N_{node}$ ). The observed data with error bars are shown as orange points, and the shaded regions represent the  $1\sigma$  uncertainty of the ANN reconstructions. The corresponding  $d_L(z)$  reconstruction is shown in Appendix Fig. A.1.

Here, we consider two reconstructed distance products, the luminosity distance  $d_L(z)$  and the distance modulus  $\mu(z)$ , and apply the ABC-rejection method to each of them using three distance criteria, namely (a)  $\chi^2$ , (b) Euclid, and (c) LML which are discussed earlier. The resulting posterior probabilities are summarized in Fig. A.3. For each hyperparameter labelled as  $HLi - Nj$  with  $i$  the number of hidden layers and  $j$  the number of nodes per layer, the posterior probability shown in Fig. A.3

is obtained by averaging over 10000 ABC posterior-probability evaluations, so that the bars represent ensemble-averaged preferences. For  $d_L(z)$  shown in the top panel, the  $\chi^2$ - and Euclid-based posteriors are relatively flat. Most candidates cluster around  $\sim 9\%$ - $12\%$ , indicating that these two criteria provide only weak discrimination among the surviving architectures. Moreover, the LML criterion yields a more peaked posterior, with HL2-N1024 reaching the highest probability, followed by HL1-N1024 and a group of models around the  $\sim 10\%$  level. In contrast, hyperparameters such as HL2-N4096 receive essentially zero posterior weight at 0.0% in two distance criteria.

For  $\mu(z)$  shown in the bottom panels, the trend is even more pronounced. Criteria such as  $\chi^2$  and the Euclidean distance favor only a narrow subset of hyperparameters. For example, under the  $\chi^2$  criterion both HL2-N128 and HL2-N256 receive identical weights of 17.4%, while under the Euclidean distance they each receive 13.5%. In contrast, the LML posterior is strongly concentrated, assigning 26% of the weight to HL2-N128 and HL2-N256. In contrast, hyperparameters such as HL2-N512 receive essentially zero posterior weight at 0.0% in all three distance criteria.

In order to more clearly compare the advantages and disadvantages of the two hyperparameters, we further transform the posterior distribution histogram into a Bayes factor  $\mathcal{B}_f$  between the two hyperparameters displayed in the form of heatmap in Fig. A.4 as the results of  $d_L(z)$  shown in the top panels and  $\mu(z)$  shown in the bottom panels. And the lighter the color, the larger the Bayes factor, signifying stronger evidence. The heatmaps are interpreted from the Y-axis (row model) to the X-axis (column model), where the cell at column  $i$  and row  $j$  represents the Bayes factor  $\mathcal{B}_{ij}$  defined in Eq. (A.7) under equal model priors. When forming these ratios, architectures with ABC posterior probabilities consistent with zero were excluded to avoid ill-defined or numerically unstable Bayes factors. This exclusion explains why the heatmaps may display fewer hyperparameter combinations than the full posterior histograms, as illustrated by the case of HL2-N4096 for  $d_L(z)$  and HL2-N512 for  $\mu(z)$ .

The analysis reveals a distinct contrast between the two observables. For  $d_L(z)$ , the Bayes-factor contrasts under the  $\chi^2$  and Euclidean criteria are “barely worth mentioning”, with values remaining very close to unity, consistent with the nearly flat posteriors in Fig. A.3. Even under the LML criterion, the separation remains moderate, indicating that several hyperparameters are statistically comparable once they pass the initial training-quality pre-screening. For  $\mu(z)$ , however, the Bayes factors are substantially more informative. The LML-based comparison shows clear preferences, with ratios reaching the “substantial” and “strong” regime for the most favored models. This aligns with the sharp concentration of the LML posterior on HL2-N128 and HL2-N256 observed in Fig. A.3, respectively.

Nevertheless, for a subset of the surviving hyperparameters, the Bayes factors remain close to  $\mathcal{B}_f \approx 1$ , with their ABC posterior probabilities differing only slightly. This near-degeneracy is observed, for example, among several candidates for  $d_L(z)$  with probabilities around the  $\sim 10\%$  level, and in the nearly tied cases for  $\mu(z)$  under the  $\chi^2$  and Euclidean criteria. In such situations, Bayes factors and ABC posteriors alone lack sufficient discriminative power. Therefore, we incorporated the estimated risk function defined by Eq. (A.6) and shown in Fig. 2 as the final decision criterion. Concretely, the risk heatmap for  $d_L(z)$  shows a comparatively flat landscape, with most candidates sharing a similar  $\log_{10}(\text{risk})$  value around 8.182. But, it identifies a clear minimum at HL2-N128 which  $\log_{10}(\text{risk})$  value is 8.174. In contrast, for  $\mu(z)$ , the analysis identifies a clear minimum at

HL2 – N128, which corresponds to a  $\log_{10}(\text{risk})$  value of approximately 2.144, and a similarly low value of about 2.148 at HL2 – N256. Several HL1 configurations exhibit significantly higher risk, for instance, with  $\log_{10}(\text{risk})$  values greater than 2.3. For this observable, the risk function thus serves primarily as a consistency check and tie-breaker when other criteria prove indistinguishable.

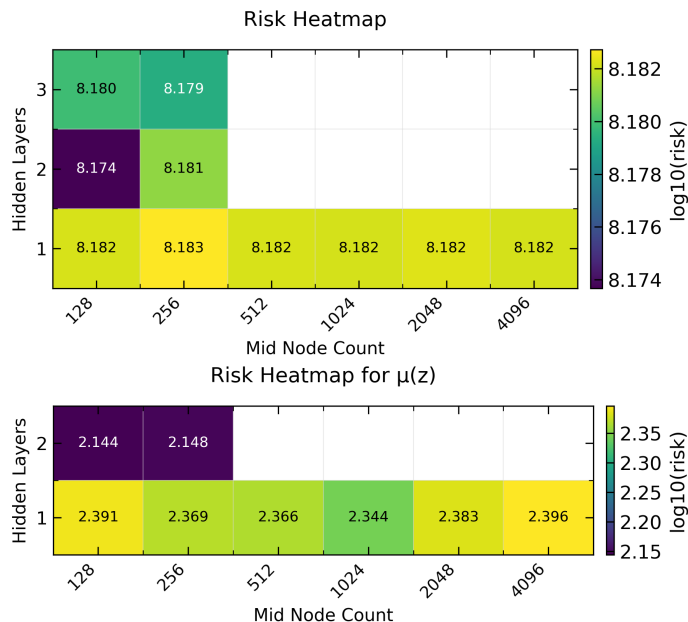


Fig. 2: The risk heatmap for luminosity distance  $d_L(z)$  (top panel) and distance modulus  $\mu(z)$  (bottom panel). The heatmaps show the log of the risk values for different combinations of hidden layers and mid-node counts in the ANN hyperparameters. The color bar represents the range of  $\log_{10}$  risk values, with purple indicating lower risk and green indicating higher risk.

Following the model selection method, we identify HL2-N128 as the optimal hyper-parameters for both  $d_L(z)$  and  $\mu(z)$ . From the ensemble of hyper-parameters satisfying the ABC rejection and risk-function criteria, we generate the final ANN reconstruction and its covariance matrix. Fig. 3 presents the resulting  $\mu(z)$  reconstruction alongside the low-redshift GRB subset ( $z \leq 1$ ). The corresponding  $d_L(z)$  comparison is provided in Appendix Fig. A.2.

#### 4. GRB Calibrations and Cosmological Constraints

This section builds on the data and reconstruction methods described above to show how we construct a GRB distance ladder based on the Amati relation and combine it with ANN reconstruction to constrain cosmological models. The procedure consists of three main steps. First, we calibrate the Amati and Combo relations using model-independent low-redshift luminosity distances reconstructed by ReFANN. Second, we use the calibrated relations to infer the luminosity distances of high-redshift GRBs. Finally, we incorporate the covariance information through the ANN likelihood together with the GRB distance information into a combined Bayesian framework to perform parameter inference within flat  $\Lambda$ CDM and  $w_0 w_a$ CDM.

Among the various empirical GRB correlations, the Amati relation is one of the most widely used. Its basic form is a power-law relation between the rest-frame spectral peak energy  $E_{p,i}$  and

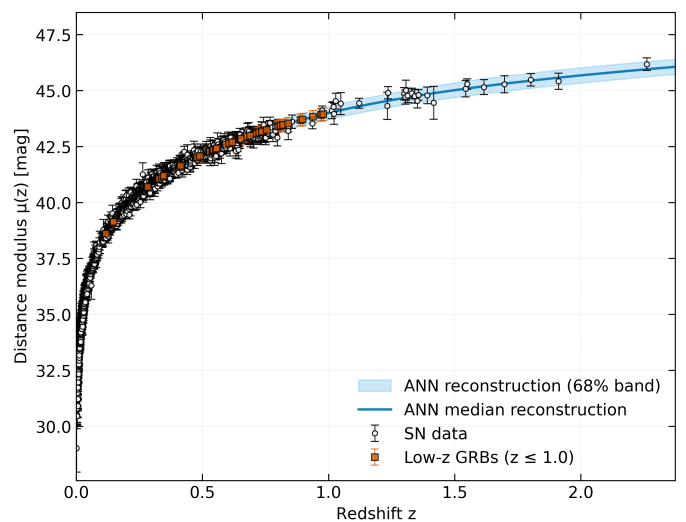


Fig. 3: Comparison between the Pantheon+ SNe Ia distance modulus  $\mu(z)$  reconstructed with the ANN and the low-redshift GRB calibration subset. The solid line represents the reconstructed relation, with the shaded band indicating the 68% reconstruction uncertainty. The SNe Ia data points are shown with their observational error bars, while the low-redshift GRBs ( $z \leq 1$ ) are overplotted to demonstrate consistency between the GRB calibration anchor and the SNe distance ladder. The corresponding  $d_L(z)$  comparison is shown in Appendix Fig. A.2.

the isotropic-equivalent radiated energy  $E_{\text{iso}}$ . In a logarithmic form, it can be written as

$$\log_{10} \left( \frac{E_{\text{iso},i}}{\text{erg}} \right) = A_A + \gamma_A \log_{10} \left( \frac{E_{p,i}}{\text{KeV}} \right) + \eta_A, \quad (8)$$

where  $A_A$  is the intercept,  $\gamma_A$  is the slope, and  $\eta_A$  denotes the intrinsic scatter of the relation. The latter is usually modelled as a Gaussian random variable with zero mean and variance  $\sigma_{v_A}^2$ , i.e.  $\eta_A \sim \mathcal{N}(0, \sigma_{v_A}^2)$ . For each GRB we have, from Sect. 2, the rest-frame peak energy Eq. (2), and the bolometric fluence  $S_{\text{bol}}$  obtained after K-correction. Given a luminosity distance  $d_L$ , the isotropic-equivalent energy follows from Eq. (6). Assuming statistical independence between different GRBs conditional on  $d_L$ , the log-likelihood for the Amati relation is

$$\ln \mathcal{L}_{\text{Amati}} = -\frac{1}{2} \sum_{i \in \mathcal{D}_{\text{cal}}} \left[ \frac{(\Delta_i^A)^2}{\sigma_{\text{tot},i}^2} + \ln \left( 2\pi (\sigma_{\text{tot},i}^A)^2 \right) \right], \quad (9)$$

where  $\mathcal{D}_{\text{cal}} = \{i | z_i \leq z_{\text{cut}}\}$  denotes the calibration subsample,  $\Delta_i^A = \log_{10} \left( \frac{E_{\text{iso},i}}{\text{erg}} \right) - A_A - \gamma_A \log_{10} \left( \frac{E_{p,i}}{\text{KeV}} \right)$  and  $(\sigma_{\text{tot},i}^A)^2 = \sigma_{\log_{10} E_{\text{iso},i}}^2 + \gamma_A^2 \sigma_{\log_{10} E_{p,i}}^2 + (\sigma_{\text{int},\text{cal}}^A)^2$ . Similarly, the log-likelihood for the Combo relation is

$$\ln \mathcal{L}_{\text{Combo}} = -\frac{1}{2} \sum_{i \in \mathcal{D}_{\text{cal}}} \left[ \frac{(\Delta_i^C)^2}{\sigma_{\text{tot},i}^2} + \ln \left( 2\pi (\sigma_{\text{tot},i}^C)^2 \right) \right], \quad (10)$$

where  $\Delta_i^C = \log_{10} \left( \frac{L_{0,i}}{\text{erg s}^{-1}} \right) - \log_{10} \left( \frac{A_C}{\text{erg s}^{-1}} \right) - \gamma_C \left[ \log_{10} \left( \frac{E_{p,i}}{\text{keV}} \right) - \log_{10} \left( \frac{\tau_i/s}{|1+\alpha_i|} \right) \right]$ , and the total variance is given by  $(\sigma_{\text{tot},i}^C)^2 = \sigma_{\log_{10} L_{0,i}}^2 + \gamma_C^2 (\sigma_{\log_{10} E_{p,i}}^2 + \sigma_{\log_{10} \tau_i}^2 + \sigma_{\log_{10} |1+\alpha_i|}^2) +$

$(\sigma_{\text{int,cal}}^C)^2$ . To model residual variance beyond the measured uncertainties and intrinsic GRB scatter, we introduce an intrinsic scatter parameter  $\sigma_{\text{cal}}$ . This term is added in quadrature to the GRB distance uncertainties in the cosmological likelihood, absorbing potential unmodeled systematic effects from calibration and inference.

As discussed earlier, the ReFANN network provides a cosmology-independent reconstruction of the SNe Ia luminosity distance  $d_L(z)$  and distance modulus  $\mu(z)$  from the Pantheon+ sample, along with associated predictive uncertainties. To balance data usage and robustness, we split the GRB sample at  $z_{\text{cut}} = 1$ , motivated by the fact that Pantheon+ contains a dense and precise set of SNe Ia at  $z < 1$  where the ReFANN reconstruction is most reliable. This ensures that the distances used to calibrate low-redshift GRBs depend minimally on extrapolation beyond the SNe Ia redshift range. To assess sensitivity to this specific choice, we repeated the full analysis for  $z_{\text{cut}} = 0.8$  and 1.2. The results are discussed in Sect. 5 and presented in Appendix C.

A fundamental and physically well-motivated assumption for this calibration is that two sources at the same redshift, such as an SNe Ia and a GRB, share the same luminosity distance. This assumption follows directly from the cosmological principle of homogeneity and isotropy. Based on this assumption, we treat the ANN predictions at the redshifts of low- $z$  GRBs as the expected distances for these events. In our paper, these predictions are described by a multivariate normal (MVN) distribution with a full covariance matrix, capturing both the individual uncertainties and the correlations between predictions at different redshifts

$$\mathbf{d}_{L,\text{cal}}^{\text{ANN}} \sim \mathcal{N}(\bar{\mathbf{d}}_{L,\text{cal}}^{\text{ANN}}, \mathbf{C}_{L,\text{cal}}^{\text{ANN}}), \quad (\text{Amati}), \quad (11)$$

and

$$\boldsymbol{\mu}_{\text{cal}}^{\text{ANN}} \sim \mathcal{N}(\bar{\boldsymbol{\mu}}_{\text{cal}}^{\text{ANN}}, \mathbf{C}_{\mu,\text{cal}}^{\text{ANN}}), \quad (\text{Combo}). \quad (12)$$

We propagate the ANN reconstruction uncertainty into the GRB calibration by drawing Monte Carlo realisations jointly from these MVNs, while retaining the observational errors from the GRB measurements themselves, which enter the likelihood through standard error propagation in the Amati and Combo relations. The resulting sampling dataset is obtained from MVN distributions at  $\mathbf{z}_{\text{cal}}$ , and we verify that the marginal sampling outcomes are consistent with Gaussian distributions using a  $\chi^2$  goodness-of-fit test with the rejection region  $W = \{\chi^2 > \chi_{0.95}^2\}$  (D'Agostino & Stephens 1986; Press et al. 1992; Bevington & Robinson 2003). For the Combo relation, we apply the same procedure, replacing  $d_L(z)$  with  $\mu(z)$  and updating the observational errors to include  $\sigma_{E_{p,i}}, \sigma_{F_0}, \sigma_{\tau}, \sigma_{\alpha_{pL}}$ , which are propagated identically.

We apply a consistent Monte Carlo procedure to construct high-redshift GRB distance datasets for both correlations. For each high-redshift event ( $z_j > z_{\text{cut}}$ ), we draw a large number of correlation parameters from their joint posterior and, for each draw, combine the observed GRB data with their uncertainties to solve for the corresponding distance measure. For the Amati relation, this yields posterior predictive samples of luminosity distance  $d_{L,j}^{(\text{high})}$  with associated uncertainties  $\sigma_{d_{L,j}}^{(\text{high})}$ . For the Combo relation, we follow an identical strategy to obtain distance modulus samples  $\mu_j^{(\text{high})}$  and  $\sigma_{\mu,j}^{(\text{high})}$ . These high-redshift estimates are then combined with the low-redshift values from the ReFANN reconstruction, producing two complete and consistently derived

GRB datasets spanning  $z \approx 0.03$  to  $z \approx 8-9$ : one from the Amati relation in the luminosity distance, and one from the Combo relation in the distance modulus

$$\left\{ \left( z_i, d_{L,i}^{(\text{low})}, \sigma_{d_{L,i}}^{(\text{low})} \right) \right\}_{z_i \leq z_{\text{cut}}} \cup \left\{ \left( z_j, d_{L,j}^{(\text{high})}, \sigma_{d_{L,j}}^{(\text{high})} \right) \right\}_{z_j > z_{\text{cut}}}, \quad (13)$$

and the other is the distance modulus dataset from the Combo correlation,

$$\left\{ \left( z_i, \mu_i^{(\text{low})}, \sigma_{\mu,i}^{(\text{low})} \right) \right\}_{z_i \leq z_{\text{cut}}} \cup \left\{ \left( z_j, \mu_j^{(\text{high})}, \sigma_{\mu,j}^{(\text{high})} \right) \right\}_{z_j > z_{\text{cut}}}. \quad (14)$$

Both correlations are processed within the same hierarchical inference framework, differing only in the chosen distance indicator and the specific GRB observables entering the likelihood.

After constructing the distance data sets, we constrain the cosmological parameters and the GRB-relation parameters within a hierarchical Bayesian analysis. For a given cosmological model, the theoretical luminosity distance can be written as (Goobar & Perlmutter 1995)

$$d_L^{\text{th}}(z; \boldsymbol{\theta}) = \frac{c(1+z)}{H_0} \int_0^z \frac{dz'}{E(z'; \boldsymbol{\theta})}, \quad (15)$$

where  $\boldsymbol{\theta}$  denotes the set of cosmological parameters. In the case of a flat  $\Lambda$ CDM model we have  $\boldsymbol{\theta} = (H_0, \Omega_m)$ , while for the  $w_0 w_a$ CDM we adopt  $\boldsymbol{\theta} = (H_0, \Omega_m, w_0, w_a)$ . In our final inference, the Pantheon+ information enters through the ANN covariance matrix, rather than an additional explicit SN term.

Given that the GRB distance indicators are inferred through an empirical correlation, the correlation parameters must be sampled jointly with the cosmological parameters, and their uncertainties including intrinsic scatter must be propagated consistently into the GRB error estimation. In this paper we treat the Amati and Combo relations as two separate calibration inferences. The Amati inference is built on the luminosity distance indicator  $d_L(z)$  inferred from  $(E_{p,i}, S_{\text{bol}})$ , whereas the Combo inference is naturally formulated in terms of the distance modulus  $\mu(z)$  through  $L_0$  and the corresponding Combo observables. Accordingly, we define two total log-likelihoods:

$$\ln \mathcal{L}_{\text{tot}}^{(\text{Amati})} = \ln \mathcal{L}_{\text{cal}}^{(d_L)} + \ln \mathcal{L}_{\text{cos}}^{(d_L, \text{high})}, \quad (16)$$

and

$$\ln \mathcal{L}_{\text{tot}}^{(\text{Combo})} = \ln \mathcal{L}_{\text{cal}}^{(\mu)} + \ln \mathcal{L}_{\text{cos}}^{(\mu, \text{high})}. \quad (17)$$

In the first case,  $\ln \mathcal{L}_{\text{cal}}^{(d_L)}$  calibrates the Amati parameters  $(A_A, \gamma_A, \sigma_{v_A})$  and cosmological parameters hierarchically

$$\ln \mathcal{L}_{\text{cal}}^{(d_L)} = -\frac{1}{2} \sum_{i \in \mathcal{D}_{\text{cal}}} \frac{(d_{L,\text{GRB},i}^{\text{obs}} - d_L^{\text{th}}(z_i; \boldsymbol{\theta}))^2}{\sigma_{\text{cal},i}^2} - \frac{1}{2} \sum_{i \in \mathcal{D}_{\text{cal}}} \ln 2\pi \sigma_{\text{cal},i}^2, \quad (18)$$

where  $\sigma_{\text{cal},i}^2 = \sigma_{\text{ANN},i}^2 + (\sigma_{\text{tot},i}^A)^2$ . While  $\ln \mathcal{L}_{\text{cos}}^{(d_L, \text{high})}$  compares the high-redshift GRB  $d_{L,\text{GRB}}^{\text{obs}}$  with the theoretical prediction  $d_L^{\text{th}}(z; \boldsymbol{\theta})$

$$\ln \mathcal{L}_{\text{cos}}^{(d_L, \text{high})} = -\frac{1}{2} \sum_{j \in \mathcal{D}_{\text{cos}}} \frac{(d_{L,\text{GRB},j}^{\text{obs}} - d_L^{\text{th}}(z_j; \boldsymbol{\theta}))^2}{\sigma_{\text{cos},j}^2} - \frac{1}{2} \sum_{j \in \mathcal{D}_{\text{cos}}} \ln 2\pi \sigma_{\text{cos},j}^2, \quad (19)$$

where  $\mathcal{D}_{\text{cos}} = \{j | z_j > z_{\text{cut}}\}$  and  $\sigma_{\text{cos},j}^2 = (\sigma_{\text{tot},j}^A)^2$ . In the second case,  $\ln \mathcal{L}_{\text{Combo}}$  plays the same role for the Combo parameters  $(A_C, \gamma_C, \sigma_{v_C})$ , and  $\ln \mathcal{L}_{\text{GRB}}^{(\mu, \text{high})}$  compares the high-redshift GRB  $\mu_{\text{GRB}}^{\text{obs}}$  with  $\mu^{\text{th}}(z; \boldsymbol{\theta})$ . Therefore, the equations of the likelihood function are similar to that of Eqs. 18 and 19, except that the luminosity distance is replaced by the distance modulus.

## 5. Results

We sample the joint posterior of cosmological parameters and the relevant correlation parameters using the affine-invariant ensemble MCMC sampler *emcee* (Goodman & Weare 2010; Foreman-Mackey et al. 2013). And we obtain the marginalised constraints shown in the corner plots, where the top panel corresponds to the  $\Lambda$ CDM fit and the bottom panel shows the  $w_0w_a$ CDM fit. The resulting posterior constraints are summarised in the corner plots shown in Figs. B.1 and B.2 for Amati and Combo relations, respectively. The results are summarized in Table 1. To verify that our conclusions are not sensitive to the specific choice of calibration threshold  $z_{\text{cut}} = 1$ , we repeated the full analysis for two alternative thresholds:  $z_{\text{cut}} = 0.8$  and  $1.2$ . For each we recalibrated both relations using only GRBs below the threshold and re-derived the cosmological constraints. The inferred parameters remain stable across all tested values. And the full results are presented in Appendix C (Figs. C.1-C.2 and Table C.1). We stress that the GRB sample does not provide an independent measurement of  $H_0$  in our analysis, as the value is instead derived from the low-redshift distances delivered by the ANN reconstruction. As a result, the GRB data primarily tighten constraints on the late-time expansion history at higher redshift.

The cosmological analysis based on the Amati relation (Fig. B.1) yields consistent posteriors. Under the  $\Lambda$ CDM assumption, it produces parameter estimates with smaller uncertainties than the Combo relation (Table 1), most notably for  $H_0$ , while the  $\Omega_m$  constraints remain broadly comparable. When extended to the  $w_0w_a$ CDM model, the posteriors broaden as expected and exhibit the characteristic degeneracy in the  $(w_0, w_a)$  parameter space. The Amati correlation parameters remain stable across the two models, and the inferred intrinsic scatter is consistent between them. The intrinsic scatter term is only weakly constrained and shows limited coupling to the cosmological parameters.

The Combo analysis (Fig. B.2) yields cosmological constraints consistent with those from Amati within uncertainties in  $\Lambda$ CDM (Table 1), and the correlation parameters show the strong covariance between slope  $\gamma$  and intercept  $A$ . In  $w_0w_a$ CDM, constraints on  $(w_0, w_a)$  remain weak because of the strong parameter degeneracy, while  $H_0$  stays stable since the absolute distance scale is fixed by the low-redshift reconstruction entering the ANN likelihood rather than being set by the GRB sample alone. Amati and Combo can differ more markedly in other analyses, particularly when selection effects and systematics are handled in different ways or when larger and more homogeneous afterglow samples are available (e.g. Khadka et al. 2021). With the current data and the same hierarchical treatment of calibration uncertainty applied to both relations, the resulting cosmological posteriors are statistically consistent (Table 1).

Building upon the constraints on cosmological parameters presented above, we proceed to compare our results with the main findings reported in the recent literature. In the top panel of Fig. 4, we compare the constraints on  $H_0$  within the flat  $\Lambda$ CDM model derived from various data sets: CMB/BAO combinations (Planck2018 (Planck Collaboration et al. 2020), ACT DR6 (Louis et al. 2025; Calabrese et al. 2025; Madhavacheril et al. 2024), and DESI (Adame et al. 2025)), the local distance ladder (PantheonPlus+SH0ES (Brout et al. 2022)), and our cosmological inferences (Amati and Combo). The early Universe measurements concentrate around the value inferred from CMB data, while the local distance ladder favors a higher  $H_0$ . Our GRB constraints yield central values that are located between these two regimes.

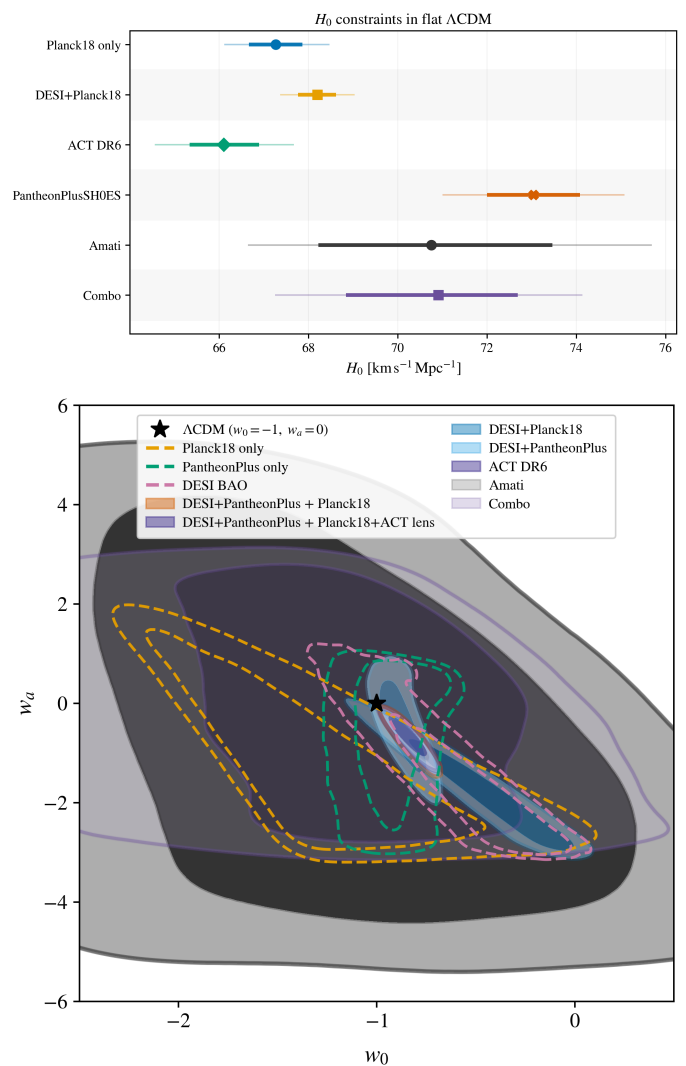


Fig. 4: Summary and comparison of our  $H_0$  and  $w_0w_a$  constraints, comparing other results with the results from Amati and Combo. The top panel shows  $H_0$  constraints in flat  $\Lambda$ CDM for Planck18 (Planck Collaboration et al. 2020), DESI+Planck18 (Adame et al. 2025), ACT DR6 (Louis et al. 2025; Calabrese et al. 2025; Madhavacheril et al. 2024), PantheonPlus+SH0ES (Brout et al. 2022), and GRBs, with thick and thin bars respectively indicating 68% and 95% credible intervals and markers indicating medians. The bottom panel shows  $(w_0, w_a)$  constraints, with filled contours for combined constraints in 68% and 95% credible intervals and dashed contours for individual constraints. The black star marks the  $\Lambda$ CDM point  $(-1, 0)$ . Amati and Combo contours are shown as lightly shaded backgrounds for comparison.

However, they exhibit considerably larger uncertainties, owing to current limitations in intrinsic scatter and calibration precision when using GRBs as distance indicators. Consequently, at the present level of precision, GRBs serve primarily as an independent consistency check for the  $H_0$  tension rather than a definitive test. The bottom panel of Fig. 4 presents constraints in the  $w_0w_a$  parameter space  $(w_0, w_a)$ . Individual data sets exhibit pronounced degeneracy directions, whereas combinations of multiple probes substantially reduce the allowed parameter region and remain compatible with the  $\Lambda$ CDM point  $(w_0, w_a) = (-1, 0)$ .

Table 1: Cosmological and correlation parameters from the Bayesian analysis of the Amati and Combo relations under  $\Lambda$ CDM and  $w_0w_a$ CDM. Quoted uncertainties are given at 68% credible intervals, with the corresponding 95% credible intervals shown in parentheses. For  $w_0w_a$ CDM, the inferred  $(w_0, w_a)$  are consistent with the  $\Lambda$ CDM limit  $(w_0, w_a) = (-1, 0)$  within the 95% credible regions.

Parameter	Amati ( $\Lambda$ CDM)	Amati ( $w_0w_a$ CDM)	Combo ( $\Lambda$ CDM)	Combo ( $w_0w_a$ CDM)
<i>Cosmological Parameters</i>				
$H_0$	$70.75^{+2.71(+4.94)}_{-2.53(-4.11)}$	$70.58^{+4.51(+9.41)}_{-3.19(-5.17)}$	$70.91^{+1.78(+3.23)}_{-2.07(-3.66)}$	$71.03^{+3.03(+6.03)}_{-2.68(-4.30)}$
$\Omega_m$	$0.553^{+0.274(+0.418)}_{-0.247(-0.410)}$	$0.588^{+0.247(+0.387)}_{-0.238(-0.472)}$	$0.531^{+0.220(+0.405)}_{-0.164(-0.281)}$	$0.552^{+0.214(+0.393)}_{-0.191(-0.437)}$
$w_0$	–	$-1.287^{+1.04(+2.02)}_{-0.993(-1.59)}$	–	$-1.174^{+0.634(+1.28)}_{-0.744(-1.54)}$
$w_a$	–	$-0.585^{+3.16(+5.09)}_{-2.96(-4.18)}$	–	$-0.030^{+1.84(+2.78)}_{-1.98(-2.81)}$
<i>Correlation Parameters</i>				
$A$	$50.06^{+0.90(+1.82)}_{-0.96(-1.98)}$	$50.07^{+0.90(+1.80)}_{-0.95(-1.93)}$	$49.75^{+0.56(+1.11)}_{-0.55(-1.12)}$	$49.79^{+0.428(+0.855)}_{-0.42(-0.836)}$
$\gamma$	$1.061^{+0.378(+0.778)}_{-0.362(-0.721)}$	$1.050^{+0.375(+0.770)}_{-0.360(-0.719)}$	$0.759^{+0.212(+0.431)}_{-0.214(-0.424)}$	$0.731^{+0.160(+0.323)}_{-0.163(-0.327)}$
<i>Intrinsic Scatter Parameters</i>				
$\sigma_{\text{cal}}$	$0.932^{+0.161(+0.337)}_{-0.138(-0.256)}$	$0.930^{+0.159(+0.331)}_{-0.138(-0.255)}$	$0.659^{+0.155(+0.330)}_{-0.133(-0.239)}$	$0.729^{+0.138(+0.292)}_{-0.119(-0.213)}$
$\sigma_{\text{cos}}$	$0.234^{+0.240(+0.500)}_{-0.163(-0.223)}$	$0.233^{+0.243(+0.507)}_{-0.162(-0.222)}$	$0.642^{+0.149(+0.312)}_{-0.127(-0.232)}$	$0.706^{+0.127(+0.269)}_{-0.113(-0.204)}$

Notes: Uncertainties are shown as  $X_{-a}^{+b(+d)}$ , where  $a, b$  correspond to the 68% credible interval and  $c, d$  to the 95% credible interval.  $H_0$  is in units of  $\text{km s}^{-1} \text{Mpc}^{-1}$ . The parameter  $A$  denotes the intercept of the corresponding correlation.  $\sigma_{\text{cal}}$  and  $\sigma_{\text{cos}}$  denote the intrinsic scatter terms used in the calibration and cosmological stages of the hierarchical inference, respectively.

within the uncertainties. In contrast to the results from BAO measurements alone, which when it combined with other probes tend to shift the parameters toward the dynamical dark energy region, the GRB only CPL posteriors derived from the Amati and Combo relations are exceptionally broad, spanning a large fraction of the parameter space. This indicates that, when considering a dynamical dark energy scenario, the GRB distance moduli obtained through our ANN based calibration provide only weak constraints on  $(w_0, w_a)$  and are likely dominated by prior and parameter degeneracies. Given the breadth of the GRB only contours relative to the combined constraints from CMB, BAO, and SNe Ia data, we display them as lightly shaded background regions for clarity. This choice visually distinguishes between our results and the well-established datasets that serve as the principal contributors to the joint constraints. Nonetheless, it is important to recognize the unique role that GRBs can play: they can reach redshifts  $z > 2$  and beyond, an area that SNe Ia cannot access. This capability highlights their potential as a high redshift tools for examining dark energy behavior.

Using the GRB distance ladders inferred from the Amati and Combo relations with the low- $z$  calibration provided by the ANN reconstruction, we examine the GRB distance modulus and the corresponding distance-modulus residuals shown in Figs. B.3 and B.4. Each figure is organised as follows: the top panel shows  $\mu_{\text{GRB}}(z)$  together with the best-fitting  $\Lambda$ CDM prediction, the second panel shows  $\mu_{\text{GRB}}(z)$  for the best-fitting  $w_0w_a$ CDM model, and the third and fourth panels display the residuals  $\Delta\mu \equiv \mu_{\text{GRB}} - \mu_{\text{th}}(z; \theta)$  for  $\Lambda$ CDM and  $w_0w_a$ CDM, respectively.

In the  $\Lambda$ CDM panels (top), the low-redshift GRBs (orange) lie close to the best-fitting curve, consistent with the fact that the correlations are anchored in the low- $z$  regime through the ANN reconstruction. The high-redshift GRBs (blue) extend the Hubble diagram to  $z \sim 9$  for both relations. The Amati- and Combo-inferred  $\mu(z)$  trends are broadly consistent within uncertainties, while small differences at the highest redshifts are within the cur-

rent error budget and may reflect measurement uncertainties and intrinsic scatter.

In the  $w_0w_a$ CDM panels (second), the inferred distance–redshift relation becomes less constrained at high redshift, reflecting the additional  $(w_0, w_a)$  degeneracy. The low- $z$  GRBs remain compatible with the best-fitting curve, whereas the high- $z$  points provide the main leverage on departures from  $\Lambda$ CDM but do not yield tight constraints with the present samples.

The residual panels (third and fourth) provide a direct check for redshift-dependent systematics. For both Amati and Combo, the residuals are consistent with a symmetric scatter around zero and show no statistically significant trend with redshift under either cosmological model. This indicates that, within current uncertainties, the calibrated relations do not introduce an obvious redshift-dependent bias in the inferred distances. Any minor excursions at the highest redshifts are plausibly attributable to larger observational uncertainties and intrinsic scatter, and can be tested further with larger and more homogeneous high- $z$  samples. Moreover, differences between GRB correlations can become more pronounced once selection effects and systematics are modelled differently (Khadka et al. 2021).

Finally, Fig. 5 compares the two GRB correlations adopted in this work: the Amati relation (top panel) and the Combo relation (bottom panel). The two relations rely on different observables. The Amati relation uses prompt-emission quantities, whereas the Combo relation includes plateau and afterglow information. Both relations are anchored to the same low-redshift distance scale provided by the ANN reconstruction. The figure therefore illustrates the observational planes, the fitted relations, and the scatter model adopted in the subsequent distance inference. The high-redshift points are shown for reference using distances inferred within our pipeline and are not used as independent calibrators. In the top panel, we show  $\log E_{\text{iso}}$  versus  $\log E_{p,i}$ , with low-redshift calibrators marked in orange and high-redshift GRBs in blue. The error bars include measurement uncertainties and the propagated distance uncer-

tainty from the reconstruction and calibration stage. The black line denotes the best-fit Amati relation, and the grey band indicates the  $1\sigma$  intrinsic scatter modelled in the hierarchical analysis (Table 1). The bottom panel shows the Combo relation in the parameter space of  $\log L_0$  versus the standardised variable  $\log(E_{p,i}/\text{keV}) - 1.46 \log[(\tau/s)/|1 + \alpha|]$ , again distinguishing low-redshift and high-redshift subsamples. The solid line gives the best-fit relation, the grey band indicates the  $1\sigma$  intrinsic scatter, and the dashed lines mark the  $3\sigma$  range to visualise the dispersion relevant for extrapolation to higher redshift. In the GRB-cosmology literature, Amati and Combo can perform differently because of their distinct observables, sample sizes, and sensitivity to selection effects and outliers (e.g. Khadka et al. 2021). In our analysis, the cosmological posteriors inferred from the two relations are broadly consistent. This does not imply that the correlations are physically equivalent. Rather, both relations share the same low-redshift anchor, are treated within the same hierarchical uncertainty-propagation scheme, and the current high-redshift leverage is limited by the size and quality of available samples, particularly for plateau measurements. As a result, the main differences at present are expressed through the inferred intrinsic scatters, while the cosmological constraints remain consistent within the current uncertainties (Table 1).

## 6. Discussion

Our methodology consists of two steps. First, we use ReFANN to reconstruct  $d_L(z)$  and  $\mu(z)$  from Pantheon+ data, providing calibration anchors for the Amati and Combo analyses. To avoid implicit priors, we implement a model selection scheme combining ABC rejection based on  $\chi^2$ , Euclidean distance, and approximate log marginal likelihood with risk function evaluation. This identifies HL2-N128 as optimal for both reconstructions. The final reconstructions incorporate observational errors and intrinsic model variance. Second, we calibrate the Amati and Combo relations using these distances. The GRB sample is split at  $z_{\text{cut}} = 1$  to minimize extrapolation errors. For each low-redshift GRB, the ANN reconstruction distance and its uncertainty are treated as a Gaussian, with Monte Carlo sampling propagating these errors into the likelihood. The intrinsic scatters  $\sigma_{v_A}$  and  $\sigma_{v_C}$  are free parameters, ensuring full uncertainty propagation. The resulting posterior distributions of the correlation parameters are then used to infer distances for high-redshift GRBs via posterior predictive sampling, yielding a final GRB distance modulus with complete error propagation.

We derive cosmological constraints from a combined hierarchical Bayesian analysis that simultaneously incorporates both the Pantheon+ and the GRB distances, together with the GRB relation parameters, ensuring self-consistent propagation of all uncertainties. Under flat  $\Lambda$ CDM, the Amati relation yields tighter constraints on both  $H_0$  and  $\Omega_m$  than the Combo relation. This difference likely arises because the Amati relation accounts for the ANN reconstruction uncertainty in  $d_L(z)$ , while the Combo relation uses  $\mu(z)$ . Although mathematically equivalent, their error propagation and effective weighting differ with finite heteroscedastic data, leading to variations in the derived constraints. When extended to  $w_0 w_a$ CDM, both relations give weak constraints on the dark energy equation-of-state parameters, with results remaining statistically consistent with  $\Lambda$ CDM. The complete numerical results are summarized in Table 1.

The joint analysis reveals the expected parameter degeneracies, notably an elongated correlation in the  $(w_0, w_a)$  parameter space for the  $w_0 w_a$ CDM model. The Hubble constant  $H_0$  remains stable across both cosmological models, with variations

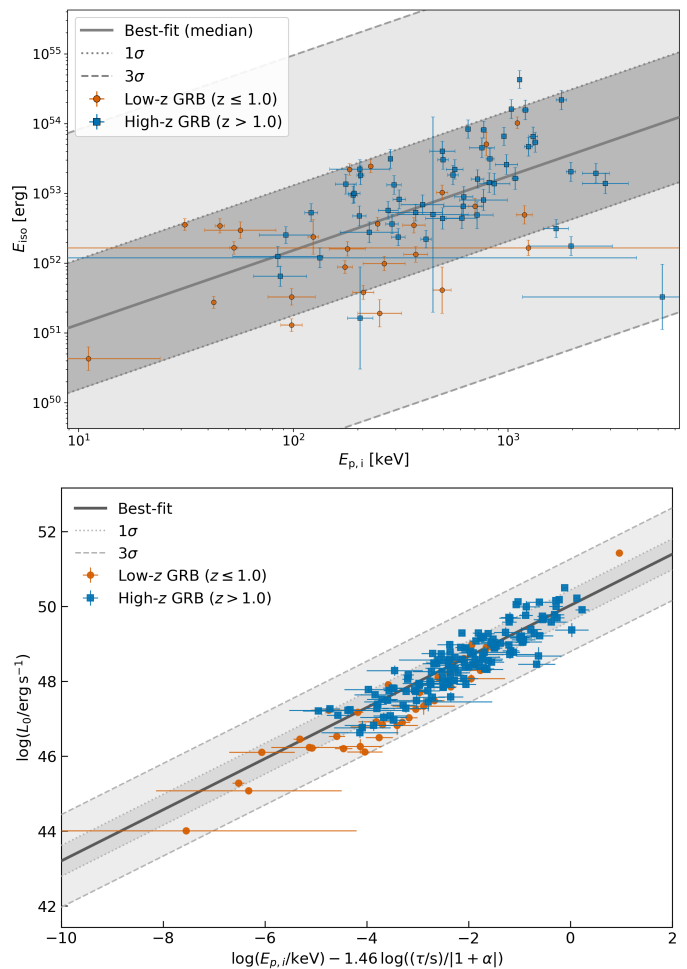


Fig. 5: Empirical correlations standardizing GRBs as distance indicators. Both panels share the same symbol and color scheme to distinguish between low-redshift and high-redshift GRBs, plotted alongside their measurement uncertainties. The top panel illustrates the Amati relation between the isotropic equivalent energy,  $E_{\text{iso}}$ , and the intrinsic peak energy,  $E_{p,i}$ . The bottom panel presents the Combo correlation in the parameter space of  $\log L_0$  versus  $\log[E_{p,i}/\text{keV}] - 1.46 \log[(\tau/s)/|1 + \alpha|]$ . In each panel, the solid line indicates the best-fit correlation, with the grey shaded bands marking the corresponding  $1\sigma$  and  $3\sigma$  intrinsic scatter regions.

below  $5 \text{ km s}^{-1} \text{ Mpc}^{-1}$ . This stability reflects the anchoring role of low-redshift Pantheon+ SNe Ia in the ANN calibration, which imprints the SNe Ia constraints onto the GRB distance ladder via the reconstructed  $d_L(z)$  relation. High-redshift GRBs, in turn, primarily constrain parameters governing late-time expansion, such as  $\Omega_m$  and the dark energy equation of state. The inclusion of high-redshift GRBs extends the distance-redshift relation well beyond current SNe Ia samples, providing a valuable anchor for probing late-time expansion. Although the present GRB sample does not tightly constrain dynamical dark energy, as evidenced by broad  $w_a$  posteriors, it complements low-redshift data and helps partially break degeneracies in the  $(w_0, w_a)$  parameter space.

A closer examination reveals distinct characteristics of the two GRB correlations. The Amati relation relies only on prompt-emission observables, namely  $E_{p,i}$  and  $S_{\text{bol}}$ , and requires a comparatively larger intrinsic scatter term in the calibration  $\sigma_{\text{cal}}$ . In

contrast, the Combo relation incorporates additional afterglow plateau information ( $L_0, \tau, \alpha$ ) and exhibits a smaller calibration intrinsic scatter term, indicating a tighter empirical relation once more burst physics is included in the standardization. However, the cosmological constraining power of Combo at high redshift is presently limited by the smaller subsample of GRBs with well-measured plateau properties and by the heterogeneous uncertainty budget of afterglow observables. These limitations propagate into the cosmological stage through  $\sigma_{\text{cos}}$  and the observational errors, and can lead to posterior uncertainties on  $\Omega_m$  that are not markedly smaller than those obtained from Amati. As a consequence, after propagating calibration and cosmological parameter uncertainties consistently in the hierarchical Bayes analysis through  $\sigma_{\text{cal}}$  and  $\sigma_{\text{cos}}$ , the cosmological posteriors inferred from the Amati and Combo relations appear similar at the present level of precision.

The agreement between the two GRB relations is noteworthy not only for its consistency but also for its physical implications. Because the Amati and Combo relations probe fundamentally different phases of the GRB emission, their concordance provides astrophysical support for the standardizable-candle hypothesis and alleviates concerns that our cosmological constraints are driven by a single potentially biased correlation. This behaviour is also consistent with the broader picture that more pronounced differences among GRB correlations may emerge once larger, more homogeneous samples and more detailed treatments of selection effects become available (Khadka et al. 2021).

The robustness of our calibration is supported by the stability of GRB correlation parameters across different background cosmologies and the absence of statistically significant redshift-dependent trends in the residuals, confirming the reliability of these empirical relations as distance indicators over a wide redshift range despite their intrinsic scatter.

Our results are consistent with  $\Lambda$ CDM and do not rule out  $w_0w_a$ CDM. This aligns with recent DESI studies showing that apparent preferences for dynamical dark energy can be sensitive to data selection and modeling assumptions, and weaken under conservative treatments of specific BAO datasets (Carloni et al. 2025; Luongo & Muccino 2024). They also agree with model-independent GRB analyses that find no strong evidence against a cosmological constant when calibration uncertainties are properly propagated (Luongo & Muccino 2020). Conversely, studies calibrating GRB correlations directly against DESI, OHD, or BAO data can favour mildly evolving dark energy solutions in some setups, with the inferred preference depending on data combinations and model selection criteria (Alfano et al. 2024, 2025). These comparisons suggest that the diversity of conclusions in the recent literature likely reflects differences in calibration strategies and dataset choices, rather than constituting robust evidence for  $w(z)$  evolution at present.

Several limitations of our approach should nevertheless be kept in mind. The ANN reconstruction, while flexible, remains an empirical interpolator, and Bayesian neural networks could offer a more principled treatment of predictive uncertainties. We have also assumed redshift-independent intrinsic scatter; a more realistic parameterization, such as  $\sigma_v(z)$ , would allow direct tests of possible evolution in the GRB population or in the correlations themselves. In addition, the flux threshold of the Fermi/GBM detector likely introduces selection effects by truncating the observed distributions in the  $E_{p,i}-E_{\text{iso}}$  and  $L_0-E_{p,i}$  planes. Explicitly modeling this selection function within the likelihood, for instance through survival analysis or Bayesian truncation methods, should reduce possible biases in the inferred correlation parameters and their scatter.

## 7. Conclusions

In this paper, we combine the Pantheon+ sample of SNe Ia, an ANN optimized through approximate Bayesian computation rejection and a dedicated risk function, and two empirical GRB correlations, namely the Amati and Combo relations. From our analysis, a number of significant results emerge:

(i) Our methodology calibrates GRB correlations without assuming a cosmological model and is based on an ANN distance reconstruction, thus mitigating the circularity problem. The resulting distance ladder extends cosmological measurements up to redshift  $z \sim 9$ .

(ii) Using two independent GRB correlations, the Amati and Combo relations, we obtain mutually consistent cosmological constraints. Although still characterized by significant uncertainties, these results appear to support the current cosmological scenario. The consistency between correlations that probe fundamentally different phases of the GRB emission, namely the prompt phase and the afterglow plateau, also provides astrophysical support for the standardizable-candle hypothesis.

(iii) The inferred  $H_0$  is consistent with both early- and late-Universe measurements within the current uncertainties, which remain large. It is important to note that the absolute distance scale is ultimately anchored to the SNe Ia cosmology through the ANN reconstruction of Pantheon+ data.

(iv) Although the high-redshift GRB data tend to favour relatively large values of  $\Omega_m$  ( $\sim 0.5$ ), the uncertainties remain significant and this result should be interpreted with caution. A larger matter density would imply a stronger deceleration at early epochs, potentially leading to tension with other observational indications of rapid structure formation in the early Universe. This suggests that the apparent preference for higher  $\Omega_m$  may reflect current statistical uncertainties and systematic effects affecting GRB cosmology, rather than a genuine cosmological signal.

(v) The present analysis is mainly limited by the small size of the available high-redshift GRB sample and by residual selection effects, particularly Malmquist bias. With a larger number of well-observed high- $z$  GRBs from ongoing and future missions such as SVOM (Paul et al. 2011; Wei et al. 2016; Atteia et al. 2022) and THESEUS (Amati et al. 2018; Stratta et al. 2018; Amati et al. 2021a,b), the statistical uncertainties on the cosmological parameters are expected to decrease. This will make it possible to assess more reliably whether the current preference for relatively high  $\Omega_m$  is physical or instead caused by limited statistics and residual systematics. Further progress will also require improved modeling of selection effects, together with cross-checks against other high-redshift probes, including BAO and future gravitational-wave standard sirens.

*Acknowledgements.* Luca Izzo acknowledges financial support from the INAF Data Grant Program 'YES' (PI: Izzo) *Multi-wavelength and multi messenger analysis of relativistic supernovae*. Tong-Jie Zhang is supported by National SKA Program of China, No. 2022SKA0110202, and the China Manned Space Program with grant No. CMS-CSST-2025-A01. Wei Hong is supported by China Scholarship Council (File No.202506040057)

## References

- Abdesslem, A. B., Dervilis, N., Wagg, D. J., & Worden, K. 2017, *Frontiers in Built Environment*, 3
- Adame, A. G., Aguilar, J., Ahlen, S., et al. 2025, *J. Cosmology Astropart. Phys.*, 2025, 021
- Alfano, A. C., Luongo, O., & Muccino, M. 2024, *J. Cosmology Astropart. Phys.*, 2024, 055
- Alfano, A. C., Luongo, O., & Muccino, M. 2025, *Journal of High Energy Astrophysics*, 46, 100348

- Alsing, J., Charnock, T., Feeney, S., & Wandelt, B. 2019, *MNRAS*, 488, 4440
- Alsing, J., Wandelt, B., & Feeney, S. 2018, *MNRAS*, 477, 2874
- Amati, L. 2006, *MNRAS*, 372, 233
- Amati, L., D'Agostino, R., Luongo, O., Muccino, M., & Tantalò, M. 2019, *MNRAS*, 486, L46
- Amati, L. & Della Valle, M. 2013, *International Journal of Modern Physics D*, 22, 1330028
- Amati, L., Frontera, F., Tavani, M., et al. 2002, *A&A*, 390, 81
- Amati, L., Guidorzi, C., Frontera, F., et al. 2008, *MNRAS*, 391, 577
- Amati, L., O'Brien, P., Götz, D., et al. 2018, *Advances in Space Research*, 62, 191
- Amati, L., O'Brien, P. T., Götz, D., Bozzo, E., & Santangelo, A. 2021a, *arXiv e-prints*, arXiv:2102.08702
- Amati, L., O'Brien, P. T., Götz, D., et al. 2021b, *Experimental Astronomy*, 52, 183
- Atteia, J.-L., Cordier, B., & Wei, J. 2022, *International Journal of Modern Physics D*, 31, 2230008
- Band, D., Matteson, J., Ford, L., et al. 1993, *ApJ*, 413, 281
- Beaumont, M. A. 2019, *Annual Review of Statistics and Its Application*, 6, 379
- Beaumont, M. A., Cornuet, J.-M., Marin, J.-M., & Robert, C. P. 2008, *arXiv e-prints*, arXiv:0805.2256
- Bernardini, M. G., Margutti, R., Zaninoni, E., & Chincarini, G. 2012, *MNRAS*, 425, 1199
- Bernardo, R. C. & Levi Said, J. 2021, *J. Cosmology Astropart. Phys.*, 2021, 027
- Bevington, P. R. & Robinson, D. K. 2003, *Data reduction and error analysis for the physical sciences*
- Bloom, J. S., Frail, D. A., & Sari, R. 2001, *AJ*, 121, 2879
- Brout, D., Scolnic, D., Popovic, B., et al. 2022, *ApJ*, 938, 110
- Butler, N. R., Kocevski, D., & Bloom, J. S. 2009, *ApJ*, 694, 76
- Calabrese, E., Hill, J. C., Jense, H. T., et al. 2025, *J. Cosmology Astropart. Phys.*, 2025, 063
- Capozziello, S. & Izzo, L. 2010, *A&A*, 519, A73
- Cardone, V. F., Capozziello, S., & Dainotti, M. G. 2009, *MNRAS*, 400, 775
- Carlóni, Y., Luongo, O., & Muccino, M. 2025, *Phys. Rev. D*, 111, 023512
- Chen, J.-f., Zhang, T.-J., He, P., Zhang, T., & Zhang, J. 2025, *European Physical Journal C*, 85, 1005
- Chevallier, M. & Polarski, D. 2001, *International Journal of Modern Physics D*, 10, 213
- Cornuet, J.-M., Santos, F., Beaumont, M. A., et al. 2008, *Bioinformatics*, 24, 2713
- Cucchiara, A., Levan, A. J., Fox, D. B., et al. 2011, *ApJ*, 736, 7
- D'Agostini, G. 2005, *arXiv e-prints*, physics/0511182
- D'Agostino, R. B. & Stephens, M. A. 1986, *Goodness-of-fit techniques*
- Dai, Z. G., Liang, E. W., & Xu, D. 2004, *ApJ*, 612, L101
- Dainotti, M. G. & Amati, L. 2018, *PASP*, 130, 051001
- Dainotti, M. G., Del Vecchio, R., Shigehiro, N., & Capozziello, S. 2015, *ApJ*, 800, 31
- Dainotti, M. G., Hernandez, X., Postnikov, S., et al. 2017, *ApJ*, 848, 88
- Demianski, M. & Piedipalumbo, E. 2011, *MNRAS*, 415, 3580
- Demianski, M., Piedipalumbo, E., Sawant, D., & Amati, L. 2017, *A&A*, 598, A112
- Dialektopoulos, K. F., Mukherjee, P., Said, J. L., & Mifsud, J. 2023, *European Physical Journal C*, 83, 956
- Foreman-Mackey, D., Hogg, D. W., Lang, D., & Goodman, J. 2013, *PASP*, 125, 306
- Gehrels, N., Ramirez-Ruiz, E., & Fox, D. B. 2009, *ARA&A*, 47, 567
- Ghirlanda, G., Ghisellini, G., Firmani, C., Celotti, A., & Bosnjak, Z. 2005, *MNRAS*, 360, L45
- Ghirlanda, G., Ghisellini, G., & Lazzati, D. 2004, *ApJ*, 616, 331
- Goldstein, A., Burgess, J. M., Preece, R. D., et al. 2012, *ApJS*, 199, 19
- Gómez-Valent, A. & Amendola, L. 2018, *J. Cosmology Astropart. Phys.*, 2018, 051
- Gómez-Vargas, I., Medel-Esquivel, R., García-Salcedo, R., & Vázquez, J. A. 2023, *European Physical Journal C*, 83, 304
- Goobar, A. & Perlmutter, S. 1995, *ApJ*, 450, 14
- Goodman, J. & Weare, J. 2010, *Communications in Applied Mathematics and Computational Science*, 5, 65
- Graziani, C. 2011, *New A*, 16, 57
- Gruber, D., Goldstein, A., Weller von Ahlefeld, V., et al. 2014, *ApJS*, 211, 12
- Hastings, W. K. 1970, *Biometrika*, 57, 97
- Holsclaw, T., Alam, U., Sansó, B., et al. 2010, *Phys. Rev. D*, 82, 103502
- Holsclaw, T., Alam, U., Sansó, B., et al. 2011, *Phys. Rev. D*, 84, 083501
- Hong, W., Jiao, K., Wang, Y.-C., Zhang, T., & Zhang, T.-J. 2023, *ApJS*, 268, 67
- Huterer, D. & Starkman, G. 2003, *Phys. Rev. Lett.*, 90, 031301
- Hwang, S.-g., L'Huilier, B., Keeley, R. E., Jee, M. J., & Shafieloo, A. 2023, *J. Cosmology Astropart. Phys.*, 2023, 014
- Izzo, L., Capozziello, S., Covone, G., & Capaccioli, M. 2009, *A&A*, 508, 63
- Izzo, L., Muccino, M., Zaninoni, E., Amati, L., & Della Valle, M. 2015, *A&A*, 582, A115
- Jeffreys, H. 1998, *Theory of Probability* (Oxford University Press)
- Jennings, E. & Madigan, M. 2017, *Astronomy and Computing*, 19, 16
- Kass, R. E. & Raftery, A. E. 1995, *Journal of the American Statistical Association*, 90, 773
- Kelly, B. C. 2007, *ApJ*, 665, 1489
- Khadka, N., Luongo, O., Muccino, M., & Ratra, B. 2021, *J. Cosmology Astropart. Phys.*, 2021, 042
- Liang, E. & Zhang, B. 2005, *ApJ*, 633, 611
- Liang, N., Xiao, W. K., Liu, Y., & Zhang, S. N. 2008, *ApJ*, 685, 354
- Linder, E. V. 2003, *Phys. Rev. Lett.*, 90, 091301
- Louis, T., La Posta, A., Atkins, Z., et al. 2025, *J. Cosmology Astropart. Phys.*, 2025, 062
- Luongo, O. & Muccino, M. 2020, *A&A*, 641, A174
- Luongo, O. & Muccino, M. 2021a, *Galaxies*, 9, 77
- Luongo, O. & Muccino, M. 2021b, *MNRAS*, 503, 4581
- Luongo, O. & Muccino, M. 2023, *MNRAS*, 518, 2247
- Luongo, O. & Muccino, M. 2024, *A&A*, 690, A40
- Maartens, R., Abdalla, F. B., Jarvis, M., & Santos, M. G. 2015, *arXiv e-prints*, arXiv:1501.04076
- Madhavacheril, M. S., Qu, F. J., Sherwin, B. D., et al. 2024, *ApJ*, 962, 113
- Malmquist, K. G. 1922, *Meddelanden fran Lunds Astronomiska Observatorium Serie I*, 100, 1
- Margutti, R., Zaninoni, E., Bernardini, M. G., et al. 2013, *MNRAS*, 428, 729
- Meegan, C., Lichti, G., Bhat, P. N., et al. 2009, *ApJ*, 702, 791
- Mészáros, P. 2006, *Reports on Progress in Physics*, 69, 2259
- Metropolis, N., Rosenbluth, A. W., Rosenbluth, M. N., Teller, A. H., & Teller, E. 1953, *J. Chem. Phys.*, 21, 1087
- Moresco, M., Amati, L., Amendola, L., et al. 2022, *Living Reviews in Relativity*, 25, 6
- Mosquera Cuesta, H. J., Turcati, R., Furlanetto, C., et al. 2008, *A&A*, 487, 47
- Muccino, M., Izzo, L., Luongo, O., et al. 2021, *ApJ*, 908, 181
- Muccino, M., Luongo, O., & Jain, D. 2023, *MNRAS*, 523, 4938
- Narayana Bhat, P., Meegan, C. A., von Kienlin, A., et al. 2016, *ApJS*, 223, 28
- Paciesas, W. S., Meegan, C. A., von Kienlin, A., et al. 2012, *ApJS*, 199, 18
- Paul, J., Wei, J., Basa, S., & Zhang, S.-N. 2011, *Comptes Rendus Physique*, 12, 298
- Peebles, P. J. E. 1982, *ApJ*, 263, L1
- Petrosian, V., Kitanidis, E., & Kocevski, D. 2015, *ApJ*, 806, 44
- Phillips, M. M. 1993, *ApJ*, 413, L105
- Piran, T. 2004, *Reviews of Modern Physics*, 76, 1143
- Planck Collaboration, Aghanim, N., Akrami, Y., et al. 2020, *A&A*, 641, A6
- Poolakkil, S., Preece, R., Fletcher, C., et al. 2021, *ApJ*, 913, 60
- Press, W. H., Teukolsky, S. A., Vetterling, W. T., & Flannery, B. P. 1992, *Numerical recipes in C. The art of scientific computing*
- Rasmussen, C. E. & Williams, C. K. I. 2006, *Gaussian Processes for Machine Learning*
- Ruffini, R., Muccino, M., Bianco, C. L., et al. 2014, *A&A*, 565, L10
- Salvaterra, R., Della Valle, M., Campana, S., et al. 2009, *Nature*, 461, 1258
- Salzano, V., D'Ábrowski, M. P., & Lazkoz, R. 2015, *Phys. Rev. Lett.*, 114, 101304
- Schaefer, B. E. 2007, *ApJ*, 660, 16
- Scolnic, D., Brout, D., Carr, A., et al. 2022, *ApJ*, 938, 113
- Seikel, M., Clarkson, C., & Smith, M. 2012, *J. Cosmology Astropart. Phys.*, 2012, 036
- Seikel, M., Clarkson, C., & Smith, M. 2013, *GaPP: Gaussian Processes in Python, Astrophysics Source Code Library*, record ascl:1303.027
- Shafieloo, A. 2007, *MNRAS*, 380, 1573
- Shafieloo, A., Alam, U., Sahni, V., & Starobinsky, A. A. 2006, *MNRAS*, 366, 1081
- Shafieloo, A., Kim, A. G., & Linder, E. V. 2012, *Phys. Rev. D*, 85, 123530
- Stratta, G., Ciolfi, R., Amati, L., et al. 2018, *Advances in Space Research*, 62, 662
- Sun, W., Jiao, K., & Zhang, T.-J. 2021, *ApJ*, 915, 123
- Tanvir, N. R., Fox, D. B., Levan, A. J., et al. 2009, *Nature*, 461, 1254
- Tanvir, N. R. & Jakobsson, P. 2007, *Philosophical Transactions of the Royal Society of London Series A*, 365, 1377
- Trotta, R. 2008, *Contemporary Physics*, 49, 71
- Vapnik, V. N. 1999, *IEEE Transactions on Neural Networks*, 10, 988
- von Kienlin, A., Meegan, C. A., Paciesas, W. S., et al. 2014, *ApJS*, 211, 13
- von Kienlin, A., Meegan, C. A., Paciesas, W. S., et al. 2020, *ApJ*, 893, 46
- Wang, F. Y., Dai, Z. G., & Liang, E. W. 2015, *New A Rev.*, 67, 1
- Wang, G.-J., Ma, X.-J., Li, S.-Y., & Xia, J.-Q. 2020, *ApJS*, 246, 13
- Wang, Y. & Tegmark, M. 2004, *Phys. Rev. Lett.*, 92, 241302
- Wasserman, L., Miller, C. J., Nichol, R. C., et al. 2001, *arXiv e-prints*, astro
- Wei, J., Cordier, B., Antier, S., et al. 2016, *arXiv e-prints*, arXiv:1610.06892
- Weinberg, D. H., Mortonson, M. J., Eisenstein, D. J., et al. 2013, *Phys. Rep.*, 530, 87
- Weyant, A., Schafer, C., & Wood-Vasey, W. M. 2013, *ApJ*, 764, 116
- Yonetoku, D., Murakami, T., Nakamura, T., et al. 2004, *ApJ*, 609, 935
- Yonetoku, D., Murakami, T., Tsutsui, R., et al. 2010, *PASJ*, 62, 1495
- Zhang, C.-Y., Hong, W., Wang, Y.-C., & Zhang, T.-J. 2024a, *MNRAS*, 534, 56
- Zhang, H., Wang, Y.-C., Zhang, T.-J., & Zhang, T. 2023, *ApJS*, 266, 27
- Zhang, J.-C., Hu, Y., Jiao, K., et al. 2024b, *ApJS*, 270, 23

## Appendix A: Methodological Appendix to the ANN Reconstruction

This appendix provides the full technical details supporting the ANN-based reconstruction methodology described in Sect. 3 of the main text. While the main text focuses on the distance-modulus ( $\mu$ ) results for conciseness, we present here the corresponding luminosity-distance ( $d_L$ ) reconstructions. Additionally, we include the complete ANN-selection diagnostics and provide explicit mathematical definitions for the uncertainty decomposition, ABC distance measures, and model-ranking criteria used in the ReFANN pipeline.

### A.1. Formal Definitions of the Reconstruction Framework

The main text provides a compact overview of the ANN-based reconstruction and the hyperparameter-selection workflow. Here we collect the explicit expressions for the uncertainty decomposition, the ABC distance measures, and the model-ranking criteria used in the ReFANN pipeline.

$$\sigma_{d_L, \text{ANN}}^2(z) = \sigma_{d_L, \text{data}}^2(z) + \sigma_{d_L, \text{model}}^2(z), \quad (\text{A.1})$$

where the error of the luminosity distance  $\sigma_{d_L, \text{data}}(z)$  can be obtained from Eq.(1) and  $\sigma_{d_L, \text{model}}(z)$  is the standard deviation between networks

$$\sigma_{d_L, \text{model}}(z) = \sqrt{\frac{1}{N-1} \sum_i [d_{L,i}^{(k)}(z) - \bar{d}_L(z)]^2}, \quad (\text{A.2})$$

where  $N$  is the number of the SNe Ia data and  $\bar{d}_L(z) = \frac{1}{N} \sum_i d_{L,i}^{(k)}(z)$  while  $d_{L,i}^{(k)}$  represents the predicted values of ANN.

First, within the ABC framework, we regard different networking architectures as distinct candidate models. For each network, we evaluate three summary statistics on a validation set, including the goodness of fit  $\chi^2$  (Bernardo & Levi Said 2021),

$$D_{\chi^2}^{(k)} = \sum_i \frac{[d_{L,i}^{\text{obs}} - d_{L,i}^{(k)}]^2}{\sigma_{d_{L,i}}^2}, \quad (\text{A.3})$$

where we use  $d_{L,i}^{\text{obs}}$  to represent the observed data of SNe Ia. The Euclidean distance between predictions and observations Jennings & Madigan (2017); Zhang et al. (2023),

$$D_{\text{Euclid}}^{(k)} = \frac{\sqrt{\sum_i [d_{L,i}^{\text{obs}} - d_{L,i}^{(k)}]^2}}{N}, \quad (\text{A.4})$$

And an approximate log marginal likelihood (LML) (Abdessalem et al. 2017; Gómez-Valent & Amendola 2018; Bernardo & Levi Said 2021)

$$D_{\text{LML}}^{(k)} = \frac{1}{2} \left[ \left( \mathbf{r}^{(k)} \right)^T \mathbf{C}^{-1} \mathbf{r}^{(k)} + \ln |\mathbf{C}| + N \ln(2\pi) \right], \quad (\text{A.5})$$

For a Gaussian likelihood, the residual vector for the  $k$ -th network is defined as  $\mathbf{r}^{(k)} = \mathbf{d}_L^{\text{SNe}} - \mathbf{d}_L^{(k)}$ , with the covariance matrix given by  $\mathbf{C} = \mathbf{C}_{\text{SNe}} + \sigma_{\text{int}}^2 \mathbf{I}$ . Here,  $\mathbf{C}_{\text{SNe}}$  denotes the full covariance matrix from Pantheon+,  $\sigma_{\text{int}}$  represents the extra variability of the ANN, and  $\mathbf{I}$  is the identity matrix of the same dimension as the extra variability. These statistics are combined into a distance metric that quantifies the compatibility between models

and data. Using this distance, an ABC-rejection algorithm performs accept/reject sampling over a large pool of randomly generated architectures, thereby efficiently selecting a subset of networks that are highly consistent with the Pantheon+ data. Moreover, to quantify how well different hyperparameters ( $N_{\text{hl}}, N_{\text{node}}$ ) perform for a given data set, we adopt an ABC-rejection method with an observable-dependent tolerance  $\varepsilon$  to select the preferred hyperparameters. The choice of  $\varepsilon$  is crucial and cannot be made arbitrarily.

Second, following the original ReFANN, we adopt the same risk function to further rank the models (Vapnik 1999; Wasserman et al. 2001)

$$\begin{aligned} \text{risk} &= \sum_i \text{Bias}_i^2 + \sum_i \text{Variance}_i \\ &= \sum_i [d_{L,i}^{\text{obs}} - d_{L,i}^{(k)}]^2 + \sum_{i=1} \sigma_{d_{L,i}}^2. \end{aligned} \quad (\text{A.6})$$

This scalar score balances the quality of the fit on the training set against the generalisation performance on an independent validation set, thus providing a global measure of model performance. Finally, we combine the ABC acceptance behaviour with the risk scores and Bayes factor  $\mathcal{B}_f$  comparisons to identify a small cluster of optimal ReFANN hyperparameters, which are then used in the subsequent analysis (Kass & Raftery 1995; Jeffreys 1998)

$$\mathcal{B}_f = \frac{P(\mathbf{d}_L | M_1)}{P(\mathbf{d}_L | M_2)} = \frac{P(M_1 | \mathbf{d}_L) P(M_2)}{P(M_2 | \mathbf{d}_L) P(M_1)}, \quad (\text{A.7})$$

where  $M_1$  and  $M_2$  represent alternative models, and  $\mathbf{d}_L$  denote the observed data. A result of  $\mathcal{B}_f > 1$  indicates that  $M_1$  is more supported by the data than  $M_2$ . The magnitude of  $\mathcal{B}_f$  possesses a quantitative interpretation based on probability theory (Jeffreys 1998) summarized it in Table A.1.

Table A.1: Correspondence between the Value of  $\mathcal{B}_f$  and the Strength of the Evidence

$\mathcal{B}_f$	$\log_{10} \mathcal{B}_f$	Strength of Evidence
$< 10^0$	$< 0$	Negative (supports $M_2$ )
$10^0$ to $10^{1/2} (\approx 3.16)$	0 to 1/2	Barely worth mentioning
$10^{1/2} (\approx 3.16)$ to $10^1$	1/2 to 1	Substantial
$10^1$ to $10^{3/2} (\approx 31.62)$	1 to 3/2	Strong
$10^{3/2} (\approx 31.62)$ to $10^2$	3/2 to 2	Very strong
$> 10^2$	$> 2$	Decisive

## Appendix B: Posterior Distributions and Distance Modulus Residuals

To maintain clarity in the main text, the posterior corner plots and the GRB distance modulus residual figures are presented in this appendix.

## Appendix C: Robustness of the Results to the Choice of $z_{\text{cut}}$

We repeat the full hierarchical inference by varying the GRB split redshift  $z_{\text{cut}}$  from 0.8 to 1.2. Table C.1 summarizes the resulting posterior constraints. Numbers in square brackets report the stability metric  $\Delta(p)/\sigma$  with respect to the baseline choice  $z_{\text{cut}} = 1.0$ . The posterior comparisons are shown in Figs. C.1 and C.2.

Table C.1: Robustness of the cosmological constraints against the choice of the GRB split redshift  $z_{\text{cut}}$ . Quoted uncertainties are given at 68% credible intervals, with the corresponding 95% credible intervals shown in parentheses. Numbers in square brackets report the stability metric  $\Delta(p)/\sigma \equiv |p(z_{\text{cut}}) - p(z_{\text{cut}} = 1.0)|/\sigma_p(z_{\text{cut}} = 1.0)$ , with  $\sigma_p(z_{\text{cut}} = 1.0) \equiv (\sigma_{p,+}^{68} + \sigma_{p,-}^{68})/2$ . The baseline ( $z_{\text{cut}} = 1.0$ ) entries match Table 1 and are marked as [ref].

Parameter	Amati ( $\Lambda$ CDM)	Amati ( $w_0 w_a$ CDM)	Combo ( $\Lambda$ CDM)	Combo ( $w_0 w_a$ CDM)
<i>Cosmological Parameters</i>				
$H_0$ ( $z_{\text{cut}} = 0.8$ )	$70.74^{+2.69(+4.87)}_{-2.53(-4.09)}$ [0.006]	$70.05^{+5.41(+12.00)}_{-3.18(-5.66)}$ [0.139]	$70.87^{+1.78(+3.19)}_{-2.07(-3.61)}$ [0.021]	$71.12^{+3.01(+6.06)}_{-2.56(-4.25)}$ [0.031]
$H_0$ ( $z_{\text{cut}} = 1.0$ )	$70.75^{+2.71(+4.94)}_{-2.53(-4.11)}$ [ref]	$70.58^{+4.51(+9.41)}_{-3.19(-5.17)}$ [ref]	$70.91^{+1.78(+3.23)}_{-2.07(-3.66)}$ [ref]	$71.03^{+3.03(+6.03)}_{-2.68(-4.30)}$ [ref]
$H_0$ ( $z_{\text{cut}} = 1.2$ )	$70.74^{+2.71(+4.84)}_{-2.54(-4.03)}$ [0.004]	$70.03^{+5.36(+11.40)}_{-3.18(-5.88)}$ [0.143]	$70.91^{+1.80(+3.18)}_{-2.08(-3.67)}$ [0.000]	$71.08^{+2.90(+5.97)}_{-2.60(-4.24)}$ [0.016]
$\Omega_m$ ( $z_{\text{cut}} = 0.8$ )	$0.557^{+0.272(+0.414)}_{-0.246(-0.405)}$ [0.016]	$0.613^{+0.268(+0.372)}_{-0.277(-0.502)}$ [0.102]	$0.536^{+0.223(+0.403)}_{-0.164(-0.275)}$ [0.027]	$0.549^{+0.207(+0.388)}_{-0.186(-0.436)}$ [0.014]
$\Omega_m$ ( $z_{\text{cut}} = 1.0$ )	$0.553^{+0.274(+0.418)}_{-0.247(-0.410)}$ [ref]	$0.588^{+0.247(+0.387)}_{-0.238(-0.472)}$ [ref]	$0.531^{+0.220(+0.405)}_{-0.164(-0.281)}$ [ref]	$0.552^{+0.214(+0.393)}_{-0.191(-0.437)}$ [ref]
$\Omega_m$ ( $z_{\text{cut}} = 1.2$ )	$0.552^{+0.274(+0.416)}_{-0.244(-0.403)}$ [0.003]	$0.605^{+0.265(+0.377)}_{-0.271(-0.496)}$ [0.071]	$0.532^{+0.215(+0.403)}_{-0.164(-0.279)}$ [0.004]	$0.558^{+0.200(+0.372)}_{-0.181(-0.424)}$ [0.027]
$w_0$ ( $z_{\text{cut}} = 0.8$ )	–	$-1.271^{+1.240(+2.44)}_{-1.090(-1.62)}$ [0.016]	–	$-1.225^{+0.652(+1.20)}_{-0.773(-1.50)}$ [0.074]
$w_0$ ( $z_{\text{cut}} = 1.0$ )	–	$-1.287^{+1.04(+2.02)}_{-0.993(-1.59)}$ [ref]	–	$-1.174^{+0.634(+1.28)}_{-0.744(-1.54)}$ [ref]
$w_0$ ( $z_{\text{cut}} = 1.2$ )	–	$-1.228^{+1.200(+2.35)}_{-1.120(-1.66)}$ [0.057]	–	$-1.205^{+0.627(+1.24)}_{-0.719(-1.52)}$ [0.044]
$w_a$ ( $z_{\text{cut}} = 0.8$ )	–	$-0.419^{+3.31(+5.07)}_{-3.04(-4.33)}$ [0.054]	–	$-0.005^{+1.85(+2.75)}_{-2.01(-2.84)}$ [0.013]
$w_a$ ( $z_{\text{cut}} = 1.0$ )	–	$-0.585^{+3.16(+5.09)}_{-2.96(-4.18)}$ [ref]	–	$-0.030^{+1.84(+2.78)}_{-1.98(-2.81)}$ [ref]
$w_a$ ( $z_{\text{cut}} = 1.2$ )	–	$-0.579^{+3.30(+5.14)}_{-2.99(-4.20)}$ [0.002]	–	$-0.088^{+1.88(+2.89)}_{-1.90(-2.76)}$ [0.031]
<i>Correlation Parameters</i>				
$A$ ( $z_{\text{cut}} = 0.8$ )	$50.07^{+0.90(+1.80)}_{-0.94(-1.93)}$ [0.014]	$50.11^{+0.91(+1.84)}_{-0.92(-1.90)}$ [0.050]	$49.77^{+0.57(+1.09)}_{-0.57(-1.13)}$ [0.035]	$49.80^{+0.41(+0.81)}_{-0.40(-0.84)}$ [0.015]
$A$ ( $z_{\text{cut}} = 1.0$ )	$50.06^{+0.90(+1.82)}_{-0.96(-1.98)}$ [ref]	$50.07^{+0.90(+1.80)}_{-0.95(-1.93)}$ [ref]	$49.75^{+0.56(+1.11)}_{-0.55(-1.12)}$ [ref]	$49.79^{+0.428(+0.855)}_{-0.42(-0.836)}$ [ref]
$A$ ( $z_{\text{cut}} = 1.2$ )	$49.99^{+0.91(+1.84)}_{-0.95(-1.94)}$ [0.070]	$50.06^{+0.90(+1.82)}_{-0.95(-1.94)}$ [0.051]	$49.76^{+0.56(+1.09)}_{-0.55(-1.12)}$ [0.024]	$49.77^{+0.41(+0.83)}_{-0.40(-0.82)}$ [0.056]
$\gamma$ ( $z_{\text{cut}} = 0.8$ )	$1.047^{+0.380(+0.784)}_{-0.362(-0.734)}$ [0.038]	$1.017^{+0.380(+0.786)}_{-0.355(-0.722)}$ [0.089]	$0.747^{+0.210(+0.433)}_{-0.206(-0.417)}$ [0.056]	$0.723^{+0.153(+0.312)}_{-0.152(-0.305)}$ [0.052]
$\gamma$ ( $z_{\text{cut}} = 1.0$ )	$1.061^{+0.378(+0.778)}_{-0.362(-0.721)}$ [ref]	$1.050^{+0.375(+0.770)}_{-0.360(-0.719)}$ [ref]	$0.759^{+0.212(+0.431)}_{-0.214(-0.424)}$ [ref]	$0.731^{+0.160(+0.323)}_{-0.163(-0.327)}$ [ref]
$\gamma$ ( $z_{\text{cut}} = 1.2$ )	$1.085^{+0.388(+0.792)}_{-0.354(-0.713)}$ [0.067]	$1.033^{+0.378(+0.773)}_{-0.360(-0.714)}$ [0.050]	$0.750^{+0.209(+0.426)}_{-0.213(-0.431)}$ [0.035]	$0.724^{+0.154(+0.316)}_{-0.153(-0.307)}$ [0.048]
<i>Intrinsic Scatter Parameters</i>				
$\sigma_{\text{cal}}$ ( $z_{\text{cut}} = 0.8$ )	$0.940^{+0.160(+0.334)}_{-0.137(-0.257)}$ [0.057]	$0.940^{+0.160(+0.334)}_{-0.136(-0.252)}$ [0.069]	$0.655^{+0.156(+0.333)}_{-0.136(-0.244)}$ [0.027]	$0.726^{+0.135(+0.283)}_{-0.120(-0.215)}$ [0.022]
$\sigma_{\text{cal}}$ ( $z_{\text{cut}} = 1.0$ )	$0.932^{+0.161(+0.337)}_{-0.138(-0.256)}$ [ref]	$0.930^{+0.159(+0.331)}_{-0.138(-0.255)}$ [ref]	$0.659^{+0.155(+0.330)}_{-0.133(-0.239)}$ [ref]	$0.729^{+0.138(+0.292)}_{-0.119(-0.213)}$ [ref]
$\sigma_{\text{cal}}$ ( $z_{\text{cut}} = 1.2$ )	$0.924^{+0.162(+0.338)}_{-0.137(-0.252)}$ [0.054]	$0.921^{+0.162(+0.337)}_{-0.137(-0.250)}$ [0.073]	$0.656^{+0.156(+0.333)}_{-0.134(-0.240)}$ [0.021]	$0.733^{+0.140(+0.296)}_{-0.119(-0.214)}$ [0.032]
$\sigma_{\text{cos}}$ ( $z_{\text{cut}} = 0.8$ )	$0.245^{+0.247(+0.514)}_{-0.160(-0.221)}$ [0.056]	$0.244^{+0.250(+0.525)}_{-0.159(-0.219)}$ [0.051]	$0.668^{+0.148(+0.312)}_{-0.123(-0.222)}$ [0.186]	$0.733^{+0.119(+0.251)}_{-0.103(-0.187)}$ [0.232]
$\sigma_{\text{cos}}$ ( $z_{\text{cut}} = 1.0$ )	$0.234^{+0.240(+0.500)}_{-0.163(-0.223)}$ [ref]	$0.233^{+0.243(+0.507)}_{-0.162(-0.222)}$ [ref]	$0.642^{+0.149(+0.312)}_{-0.127(-0.232)}$ [ref]	$0.706^{+0.127(+0.269)}_{-0.113(-0.204)}$ [ref]
$\sigma_{\text{cos}}$ ( $z_{\text{cut}} = 1.2$ )	$0.230^{+0.239(+0.496)}_{-0.163(-0.223)}$ [0.008]	$0.231^{+0.241(+0.505)}_{-0.162(-0.221)}$ [0.009]	$0.641^{+0.148(+0.325)}_{-0.128(-0.229)}$ [0.009]	$0.711^{+0.128(+0.273)}_{-0.112(-0.200)}$ [0.033]

Notes: Uncertainties are shown as  $X^{+b(+d)}_{-a(-c)}$ , where  $a, b$  correspond to the 68% credible interval and  $c, d$  to the 95% credible interval.  $H_0$  is in units of  $\text{km s}^{-1} \text{Mpc}^{-1}$ .

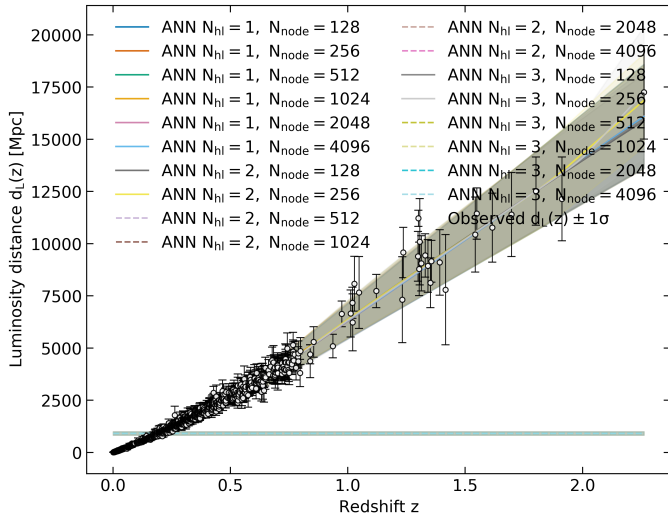


Fig. A.1: Same as Fig. 1 but for the luminosity distance  $d_L(z)$ .

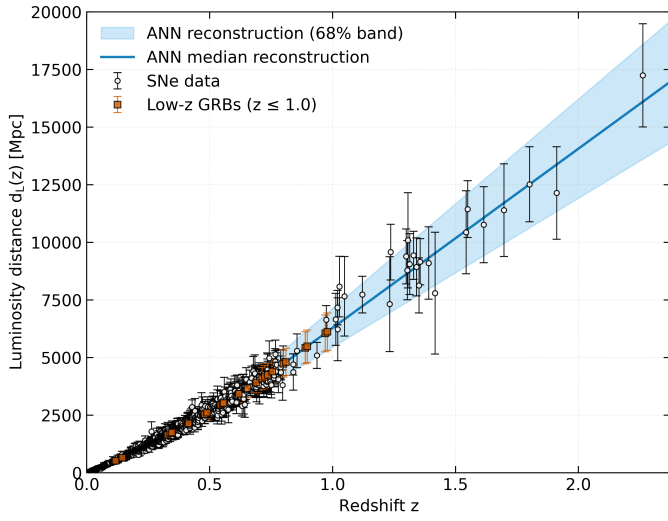


Fig. A.2: Same as Fig. 3 but for the luminosity distance  $d_L(z)$ .

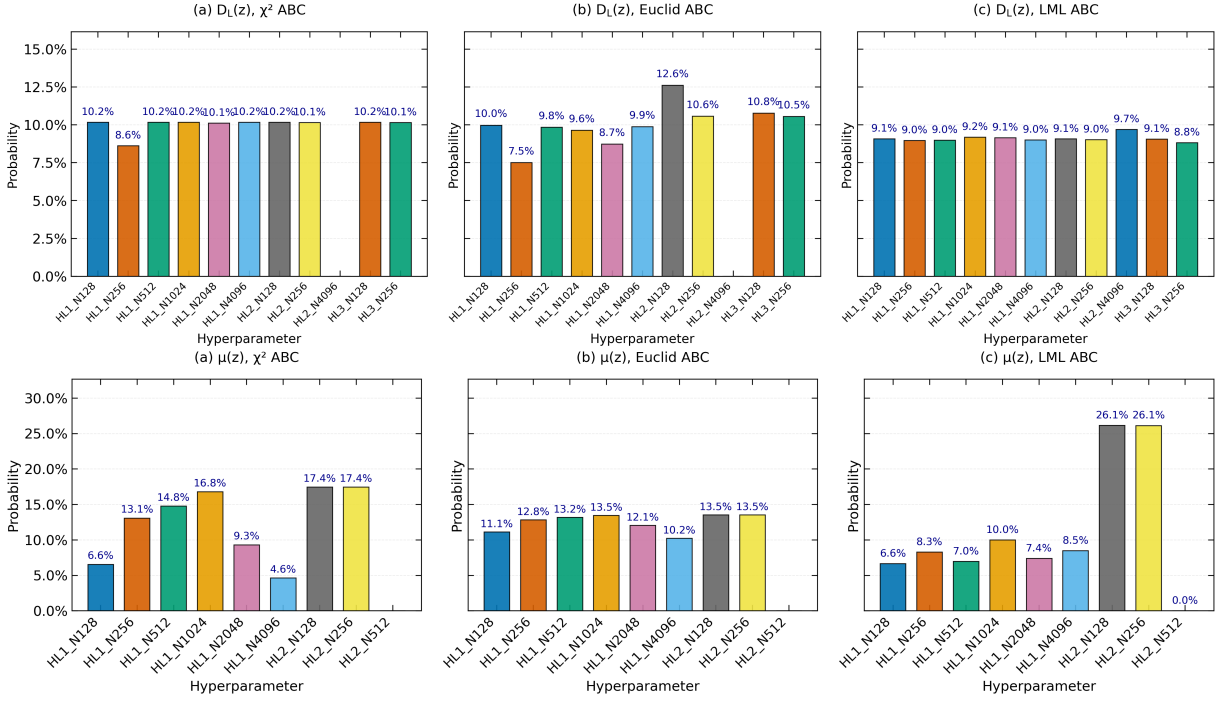


Fig. A.3: The ABC-Rejection posterior probabilities for luminosity distance  $d_L(z)$  (top panel) and distance modulus  $\mu(z)$  (bottom panel). Each subfigure corresponds to three different distance criteria: (a)  $\chi^2$  (left), (b) Euclid (middle), and (c) Log Marginal Likelihood (LML) (right). The model hyperparameters are labeled as  $HLi - Nj$ , indicating the number of hidden layers and nodes per layer. And, the values in each bar represent the posterior probabilities for each model hyperparameters.

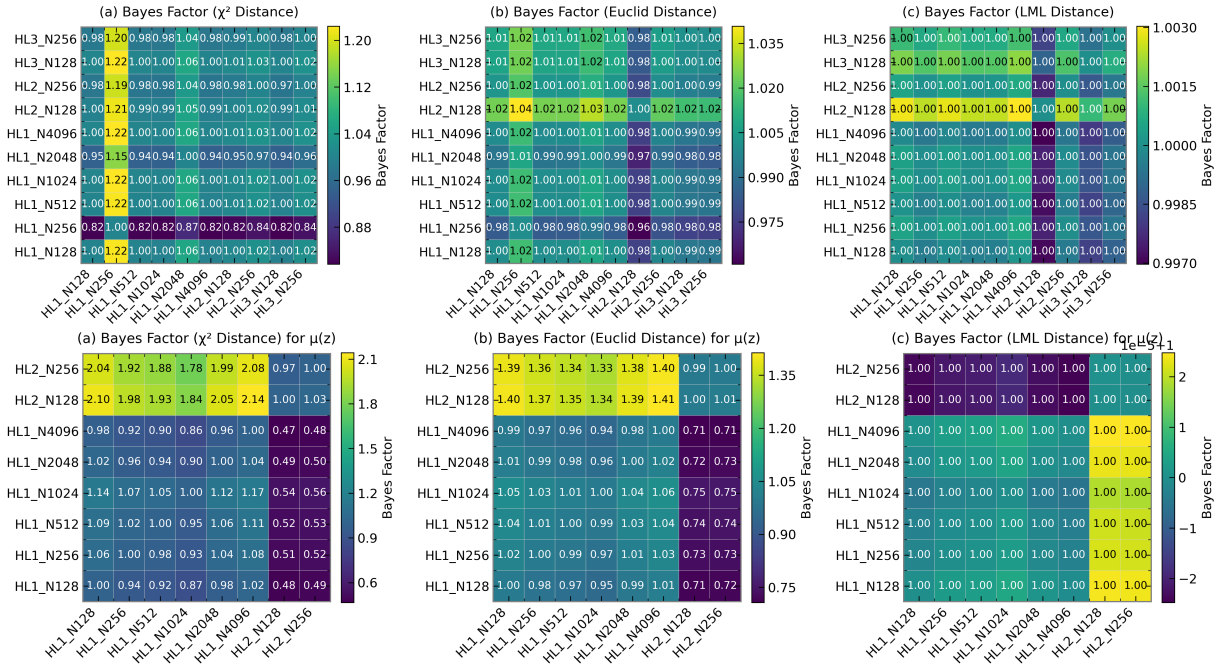


Fig. A.4: The Bayes factor comparison of ANN models for luminosity distance  $d_L(z)$  (top panel) and distance modulus  $\mu(z)$  (bottom panel) with three different distance criteria: (a)  $\chi^2$  (left), (b) Euclid (middle), and (c) Log Marginal Likelihood (LML) (right). The heatmaps display the Bayes factor values for different model architectures labeled as  $HLi - Nj$ , where the numbers represent the number of hidden layers and nodes per layer. The color bars indicate the range of Bayes factor values for each distance criterion.

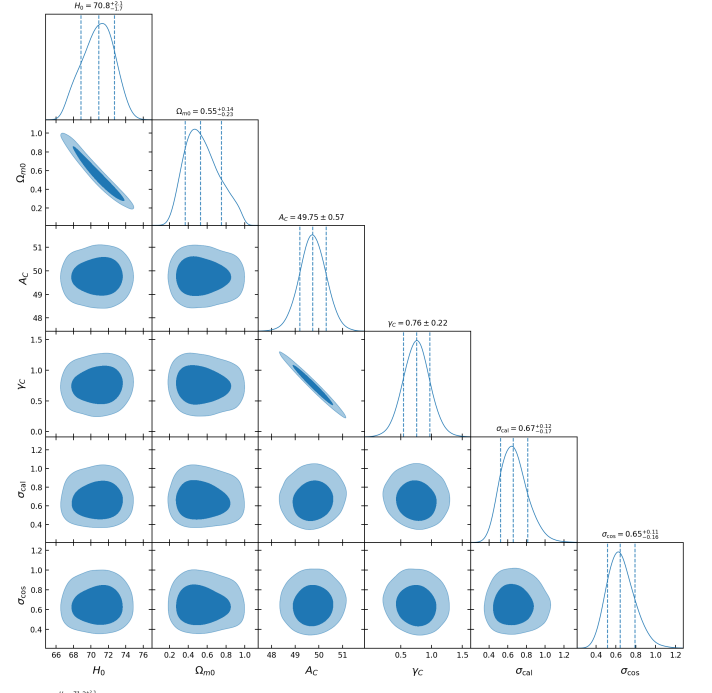
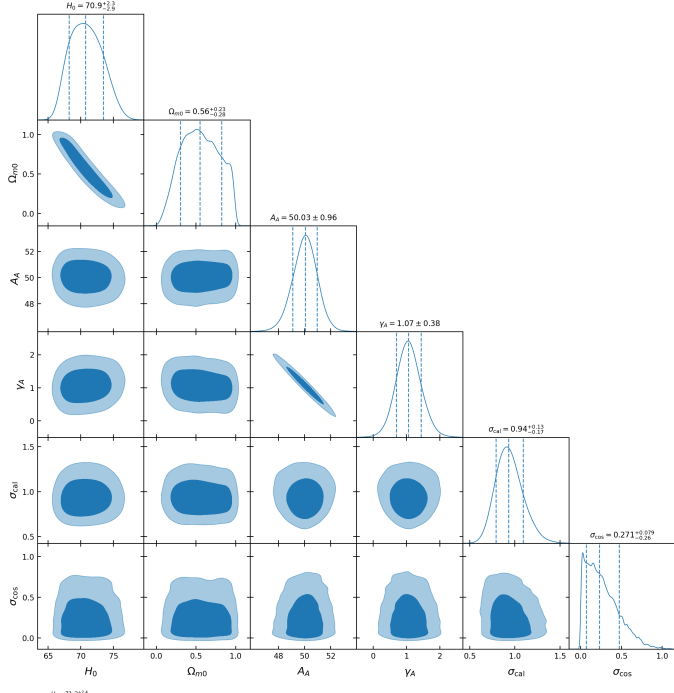


Fig. B.1: The 68%, 95%, and 99% confidence regions of the joint and marginal posterior probability distributions inferred from the hierarchical Bayesian analysis using the Amati relation. Shown are the cosmological parameters ( $H_0, \Omega_{m0}$ ) under  $\Lambda$ CDM (top panel) and ( $H_0, \Omega_{m0}, w_0, w_a$ ) under  $w_0w_a$ CDM (bottom panel), together with the correlation parameters ( $A_A, \gamma_A$ ) and the intrinsic scatter terms ( $\sigma_{\text{cal}}, \sigma_{\text{cos}}$ ) used in the calibration and cosmological parameter constraints, respectively.

Fig. B.2: Same as Fig. B.1, but for the Combo relation. The top panel shows the posterior constraints under  $\Lambda$ CDM, while the bottom panel shows those under  $w_0w_a$ CDM, including the cosmological parameters, the correlation parameters ( $A_C, \gamma_C$ ), and the intrinsic scatter terms ( $\sigma_{\text{cal}}, \sigma_{\text{cos}}$ ) for the calibration and cosmological parameter constraints, respectively.

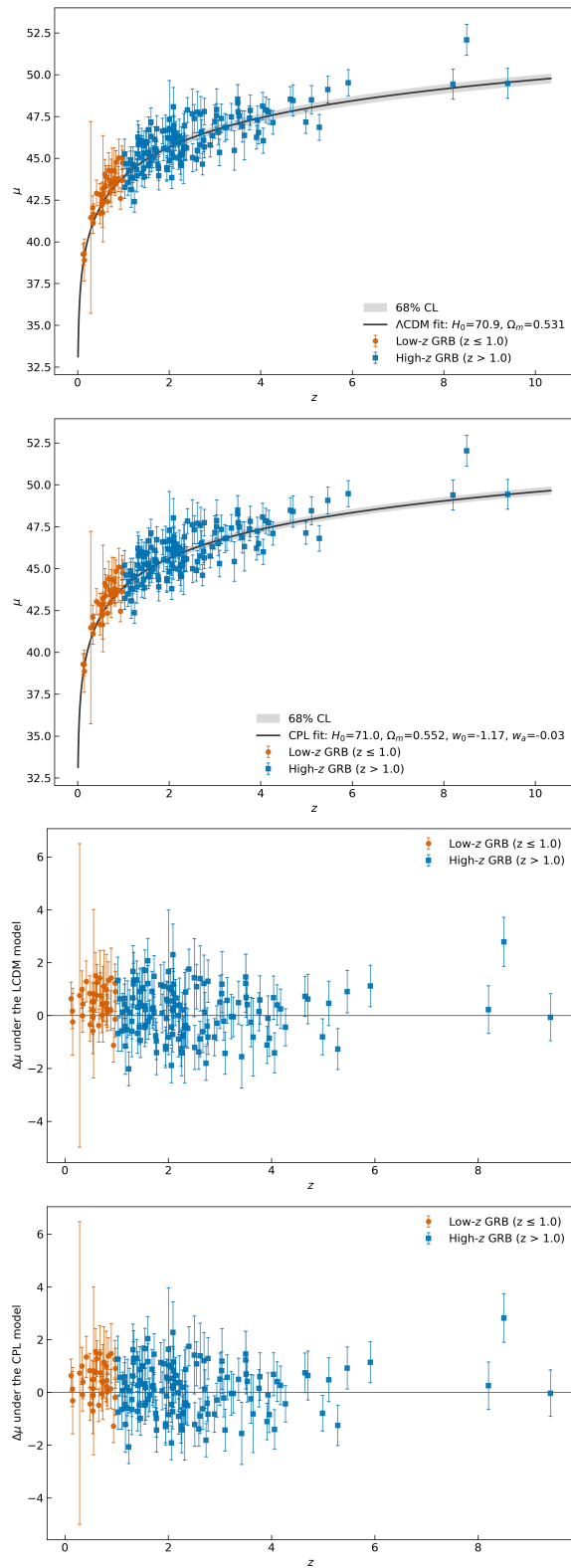
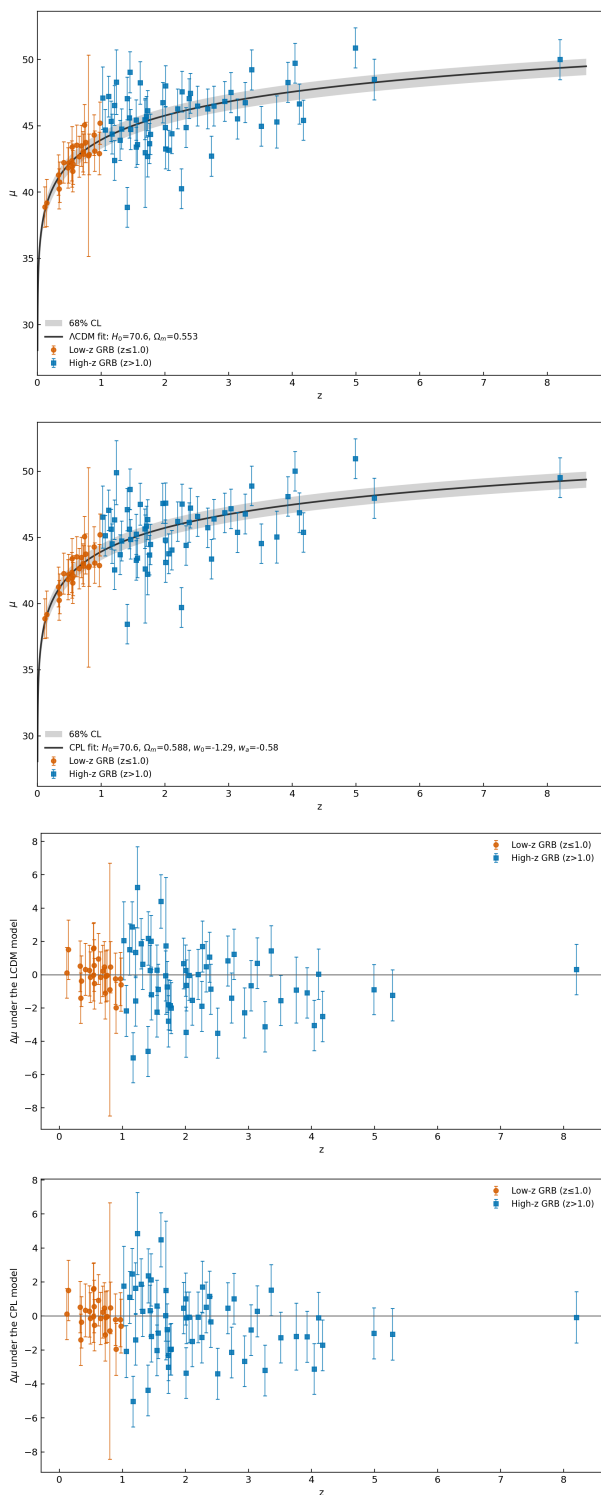


Fig. B.3: The resulting distance modulus under two cosmological models from the Amati relation. From top to bottom: the distance modulus for the  $\Lambda$ CDM model, the distance modulus for the  $w_0w_a$ CDM, the residuals  $\Delta\mu \equiv \mu_{\text{GRB}} - \mu_{\text{th}}(z; \theta)$  as a function of redshift for the  $\Lambda$ CDM model, and the residuals for the  $w_0w_a$ CDM. The distance modulus  $\mu$  of the full GRB sample are plotted against redshift together with the best-fitting curve. The residual panels provide a visual assessment of potential redshift-dependent systematic errors for each cosmology.

Fig. B.4: Same as Fig. B.3, but for the Combo relation.

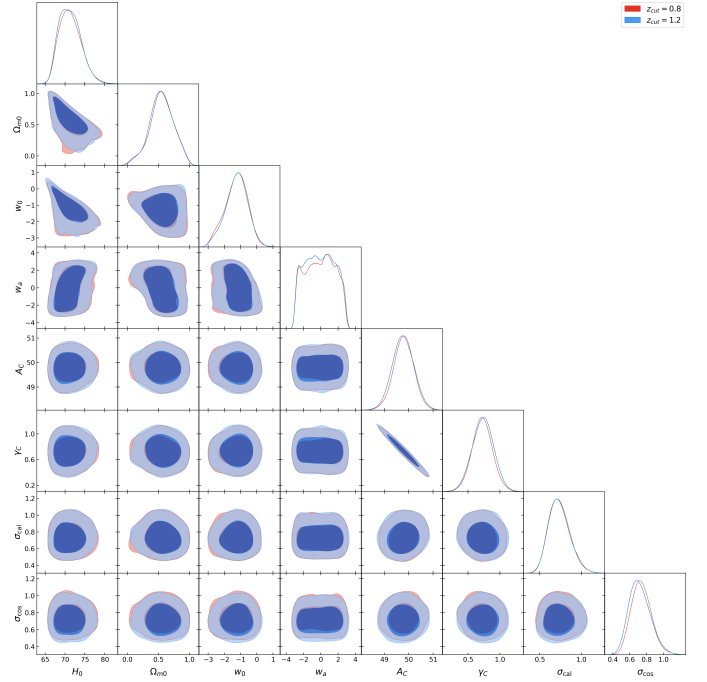
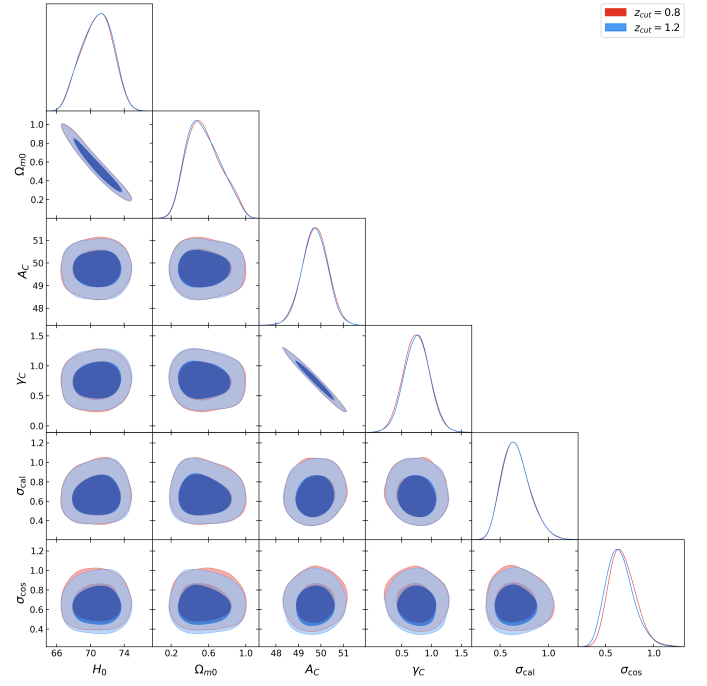
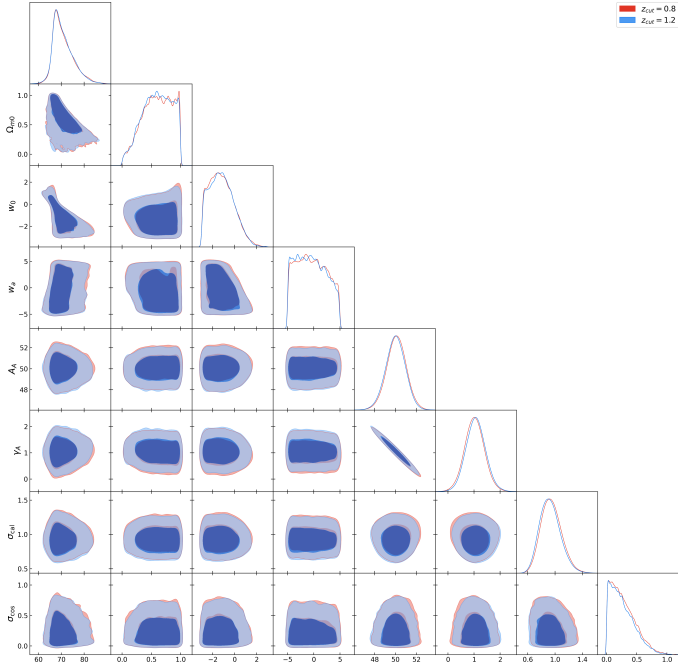
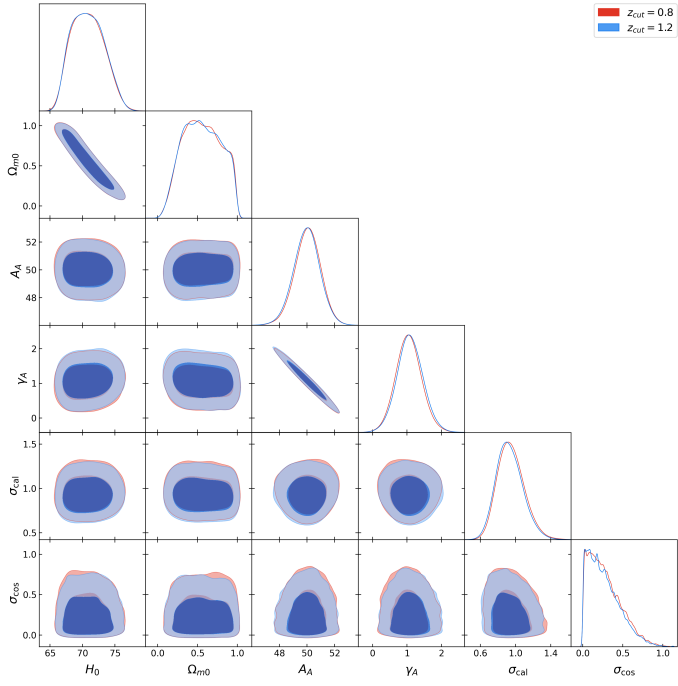


Fig. C.1: Comparison of the joint and marginal posterior distributions obtained with different choices of the GRB split redshift  $z_{\text{cut}} \in \{0.8, 1.2\}$  for the Amati relation. Shown are the 68%, 95%, and 99% credible regions for the cosmological parameters ( $H_0, \Omega_{m0}$ ) under  $\Lambda$ CDM (top panel) and for ( $H_0, \Omega_{m0}, w_0, w_a$ ) under  $w_0w_a$ CDM (bottom panel), together with the correlation parameters ( $A_A, \gamma_A$ ) and the intrinsic scatter terms ( $\sigma_{\text{cal}}, \sigma_{\text{cos}}$ ) used in the calibration and cosmological parameter inference, respectively.

Fig. C.2: Same as Fig. C.1, but for the Combo relation. We show the 68%, 95%, and 99% credible regions for the cosmological parameters under  $\Lambda$ CDM (top) and  $w_0w_a$ CDM (bottom), together with the correlation parameters ( $A_C, \gamma_C$ ) and the intrinsic scatter terms ( $\sigma_{\text{cal}}, \sigma_{\text{cos}}$ ) used in the calibration and cosmological parameter inference, respectively.